Spectroscopy and dynamics of jet-cooled hydrazines and ammonia. II. Electron-impact dissociative ionization

Jack A. Syage
The Aerospace Corporation, P. O. Box 92957/M5-754, Los Angeles, California 90009

(Received 11 May 1992; accepted 20 July 1992)

Dissociative-ionization cross sections, fragment appearance potentials, and fragment kinetic energies were measured for electron-impact excitation of jet-cooled NH_3, hydrazine (N_2H_4), and monomethyl hydrazine (MMH) over an energy range of 10–270 eV. A data base of 35 parent and fragment ions is reported. All measurements were made in a crossed electron–molecular beam apparatus using pulsed extraction and time-of-flight mass detection to ensure field-free excitation and high collection efficiency for energetic ions. Cross sections for NH_3 ionization are in good agreement with previous measurements except for ions with high kinetic energy (KE). These discrepancies are attributed to instrument-dependent KE detection efficiencies in the previous results. Cross section data have not been previously reported for N_2H_4 and MMH. The measured cross sections for total ionization at 70 eV are 2.35 $Å^2$ (NH_3), 3.76 $Å^2$ (N_2H_4), and 4.20 $Å^2$ (MMH). KE distributions were measured by an ion deflection method and gave results consistent with time-of-flight peak-shape analysis. Mean KE values $\langle \epsilon_t \rangle$ are reported for all fragment ions studied. For 170-eV excitation of NH_3, $\langle \epsilon_t \rangle$ varied from 0.026 eV (NH_2^+) to 1.4 eV (H^+). The kinetic energies for N_2H_4 and MMH fragment ions at similar excitation energies are typically much lower than for fragment ions from NH_3, conforming to statistical arguments based on density of internal states. High resolution mass spectra were recorded for MMH in order to distinguish different fragment ions of the same unit mass. Substantial rearrangement is evident for N_2H_4 and MMH dissociative ionization based on the appearance of ions such as NH_3^+ and NH_4^+ (the latter for MMH ionization only) and the magnitude of $\langle \epsilon_t \rangle$ for certain ions. The role of electronic structure and geometry on dissociation is explored using a molecular orbital analysis to predict product correlations for the excited states of $N_2H_4^+$.

I. INTRODUCTION

We have initiated a series of studies to improve on the present understanding of the spectroscopy and dynamics of hydrazine molecules. The group of molecules H_2NNRR' (R,R′=H or CH_3) is a very important class of energetic compounds that are particularly noted for their use as propellant fuels in rocket and satellite thrusters. At present, little is known about electronic states, potential energies, and excited-state correlations to dissociative products.[1–4] In the previous paper (Paper I), we recorded single-photon vacuum ultraviolet absorption and ionization spectra of NH_3, N_2H_4(hydrazine), MMH (monomethyl hydrazine), and UDMH (unsymmetrical dimethyl hydrazine) under ambient and jet-cooled collision-free conditions.[5] A molecular orbital model was developed to provide understanding of the excited states in terms of their symmetries, energy ordering, and selection rules, all as a function of geometry. Knowledge of the electronic state properties of isolated molecules is necessary to properly interpret bimolecular reaction dynamics under combustionlike conditions.[6]

In this paper we are concerned with the dissociative properties of isolated hydrazine molecules under high-energy excitation. We report absolute dissociative-ionization cross sections, fragment appearance potentials, and fragment kinetic-energy distributions for electron-impact excitation of jet-cooled NH_3, N_2H_4, and MMH over an energy range of 10–270 eV. The impetus for this work is threefold. First, NH_3 and hydrazines serve as propellants in spacecraft electrothermal thrusters using arc-heated discharges to generate high velocity. The thrust efficiency and specific impulse depend strongly on the extent of dissociation and electron–ion and atom–atom recombination. Second, electron-impact mass spectrometry is still the most practical and expedient means for analyzing gas-phase mixtures. Quantitative analysis, however, suffers from a general lack of ionization cross section data for molecules. Furthermore, detection selectivity could be improved by more accurate measurements of fragmentation patterns and branching ratios. Finally, electron impact of molecules and clusters is a rich source for producing a wide variety of ions. Ion cross section data should be of great assistance to the field of ion spectroscopy by providing a measure of the efficiency of producing unusual ions for gas-phase or matrix-isolation studies.

Energy-dependent electron-impact ionization cross sections are measured here using a crossed electron–molecular beam, time-of-flight mass spectrometer.[7–9] The apparatus employs (1) pulsed electron and molecular beams, (2) a field-free ionization volume, (3) two-stage high-voltage ion extraction, and (4) multichannel mass detection. These features account for high ion transmission, a large detector field of view, and a relative immunity to the usual mass-to-charge ratio (m/z) and kinetic-energy discrimination effects. Furthermore, the use of a molecular

 0021-9606/92/216085-23$006.00

beam sample is important for labile molecules that would otherwise decompose on surfaces (e.g., hot filaments in ion sources) if present as an ambient vapor sample.

Photoionization (PI)[10–15] and electron-impact (EI)[16–22] studies of NH_3 have been reported before. There are currently large discrepancies in the electron-impact data in terms of absolute cross sections and threshold potentials for dissociative ionization. The most reliable EI cross section measurements are currently those by Beder-ski, Wójcik, and Adamczyk (BWA),[16] Märk, Egger, and Cheret (MEC),[17] and Crowe and McConkey (CM).[18] Accurate fragment-ion threshold curves for EI ionization of NH_3 have been recorded by Morrison and Traeger[23] and by Locht *et al.*[22] The latter group also recorded KE distributions as a function of electron energy.[22] Although a consensus of data is beginning to emerge for some measurements, there still exists significant uncertainties in many of the reported cross sections and threshold potentials, particularly for weak and energetic species. We compare our cross section and threshold potentials for NH_3 to these previous studies. Satisfactory agreement is obtained in most cases, and discrepancies are usually explanable by differing instrument detection efficiencies for fragments with high kinetic energy.

Electron-impact and photoionization measurements of hydrazines are very limited.[24–31] We are not aware of any cross section measurements (either total or partial) for any hydrazine molecule. Berkowitz measured PI thresholds for the formation of $N_2H_3^+$, and $N_2H_2^+$ fragments from N_2H_4.[24,25] Foner and Hudson measured EI thresholds for $N_2H_2^+$ formation.[27] No threshold measurements for MMH dissociative ionization are available other than a very early photoionization[26] and electron-impact[28] study limited to larger fragments. All previous EI and PI studies on hydrazines were conducted on ambient vapors. The present use of a molecular beam reduces thermal energy and isolates molecules from surrounding surfaces. The collective set of cross sections, thresholds, and kinetic energies, measured for the series of molecules NH_3, N_2H_4, and MMH, has allowed us to determine the reaction mechanisms for ion fragmentation consistent with thermochemical thresholds, ion excited-state energies, and molecular-orbital correlations.

II. EXPERIMENT AND METHOD

A. Apparatus

Electron-impact ionization and dissociative-ionization cross sections were measured in a vacuum system consisting of a differentially pumped source and ionization chamber.[7,8] The source chamber contains a temperature-controlled solenoid-actuated pulsed nozzle, which is used to produce a supersonic jet expansion. The molecular beam enters the ionization chamber through a 1 mm diam. skimmer. The beam divergence is about 0.04 mrad and the beam diameter about 4 mm at the excitation region. The pulsed expansion accounts for high density at the excitation volume ($>10^{13}$ atom/cm^3) and low ambient pressure in the ionization chamber (typically $1–2\times10^{-8}$ Torr, rising to $2–5\times10^{-7}$ Torr at 50 Hz operation). The pulsed EI ion source and time-of-flight (TOF) ion optics configuration is illustrated in Fig. 1. The grids labeled V0 to V3 are each separated by 1 cm. The molecular beam traverses the region between grids V1 and V2. The drift tube length is 100 cm and the detector is a dual microchannel plate (MCP). In the following discussion we use the terms V0–V4 to designate both the ion optic components and the bias voltage applied to them.

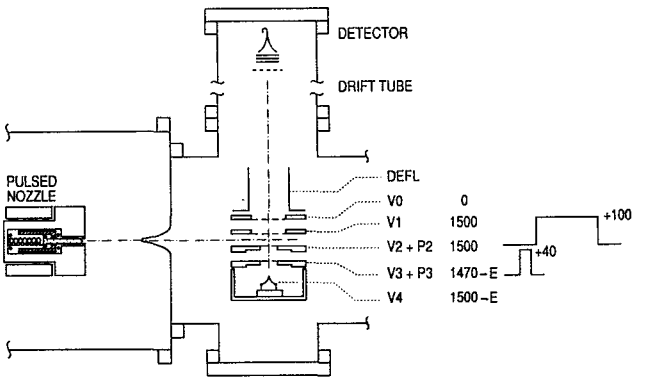

FIG. 1. Geometry and configuration of the crossed electron-molecular beam, time-of-flight mass spectrometer. The field-free excitation region is defined by the intersection of the molecular and electron beam, which is situated between parallel plate potentials V1 and V2. The electron-impact energy E is determined by the difference between the potentials applied to V1 (=V2) and V4. The electron beam is activated by applying gate pulse P3 to V3. The ions are subsequently extracted by applying pulse P2 to V2. Deflector plates (DEFL) compensate for ion drift resulting from atomic beam velocity.

Electron source. Electrons are generated by thermionic emission from a hot tungsten hairpin filament. The voltage V4 applied to the filament determines the electron energy E that impinges on the molecular beam. The electrons are prevented from exiting the source by grid V3, which is maintained at a lower potential than the filament V4. An electron beam pulse is admitted to the field-free excitation region by applying a 40 V gate pulse P3 of duration 50–500 ns to V3. The electron beam is collimated to a diameter of approximately 5 mm by the apertures at V2 and V3. The electron flux during the pulse period was varied from 0.01–1.0 μa for ion counting detection to nearly 100 μa (typically <10 μa) for current measurements.

Electron energies are scanned by ramping the voltage applied to plate V3 and filament V4. A 0–10 V control signal, generated from a 80286 computer and 12-bit D/A GPIB interface, externally controls a 0–250 V power supply which is used to float a high voltage power supply (set at fixed voltage). This arrangement permits a scanning resolution of 60 meV. The excitation region is maintained field-free during ionization. A procedure for ensuring the absence of residual fields is described elsewhere.[7] The electron energy scale is calibrated by comparing measured ionization thresholds for Ar and Ne to their known ionization potentials of 15.76 and 21.56 eV, respectively. The ions that are formed are extracted out of the ionization region by a 100 V, 4–6 μs repeller pulse P2 applied to V2. The

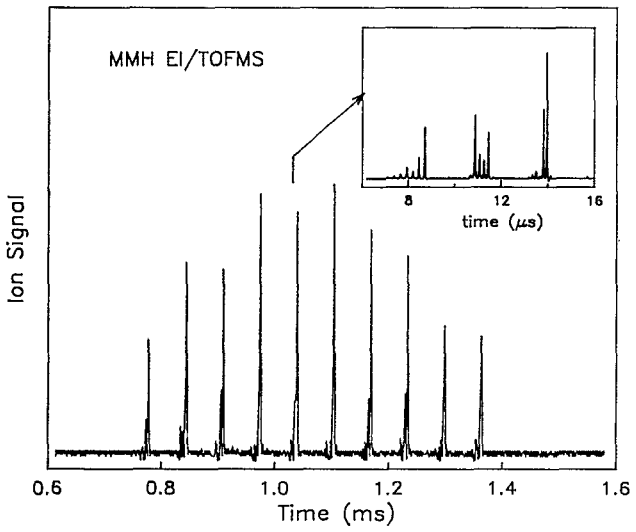

FIG. 2. Train of multiple time-of-flight mass spectra recorded for a single molecular beam pulse. Insert shows an individual TOFMS for MMH at 170 eV electron energy summed over 1000 pulses.

ions are further accelerated in the V0–V1 region to a final energy of 1550 eV before entering the field-free drift tube leading to the detector. Deflector plates are used to compensate for the molecular beam velocity orthogonal to the drift tube axis.

Signal detection. The signal at the detector anode is collected by integration (current mode) or pulse counting over gate periods spanning the distribution of TOFs for each ion. Current mode has superior sensitivity in these experiments and is used to record the ion yield vs electron energy curves. Pulse counting is used to avoid the problem of detector gain dependence on mass-to-charge ratio m/z. In this mode, the MCP detector is operated at 10^7 gain (1 kV/plate) and the anode pulses amplified by $\times 40$ and filtered by a 20 ns time constant (the latter to eliminate spurious counts due to ringing). Background counts are virtually nonexistent in the absence of the molecular beam. Current mode measurements proved to be somewhat unreliable in the threshold region because of dc offset problems obscuring the true thresholds. We therefore applied baseline correction by subtracting from the entire curve, the average intensity of several points well below the threshold. The fragment ion threshold potential represents the lowest energy at which the ion signal was judged to be greater than the baseline noise level. The threshold values are subject to kinetic shift since the finite residence time of ions in the mass spectrometer (about 2 μs) limits the time available for detecting slow dissociations.

A TOF mass spectrum is recorded in about 20 μs, whereas the molecular beam pulse typically lasts for more than 400 μs. We, therefore, allowed the EI/TOFMS pulse sequence to repeat throughout the duration of the molecular beam pulse as shown in Fig. 2. The pulse train was produced using two pulse generators; one serving as the trigger source and operating at the maximum dependable frequency for triggering the gated boxcar or ion counting systems (about 16 kHz), and the other acting as a gate or latch for the first pulse generator, allowing it to operate only over the duration of the gas pulse. The gas pulse and enabling pulse widths were operated at 600 μs in order to obtain ten spectra per gas pulse (Fig. 2). This translates to an effective repetition rate of 10×50 Hz.

High resolution mass spectra of MMH were recorded using an Extrel quadrupole mass spectrometer operating at better than 0.010 amu resolution in order to distinguish different fragments ions of same nominal mass (e.g., fragments differing by an N vs CH_2 function). Spectra were recorded for several electron energies ranging from 15 to 100 eV. The relative intensities are subject to large uncertainties due to strong KE discrimination effects for high mass resolution. Nonetheless, the results were very useful for interpreting ion dissociation mechanisms.

B. Cross section determination

Ionization cross sections, as a function of electron energy E, are obtained by measuring the ion yield of target species M relative to a well established reference species R according to the equation

$$\sigma_M(E)=\frac{I_M n_R}{I_R n_M}\sigma_R(E)\kappa_{M,R}\,, \tag{1}$$

where σ is cross section, I is ion signal intensity, and n is number density. The function $\kappa_{M,R}$ encompasses instrumental effects that may give rise to different detection efficiencies for M and R. The internal standard serving as the reference R in this work is Ar, although He and Ne standards, contained in a calibrated rare gas mixture, were also used to check our results. The Ar or rare gas mixture was flowed through a bubbler containing the sample molecule M, and the ratio n_R/n_M was determined from the Ar pressure and the vapor pressure of M at the bubbler temperature (usually 0 °C). The reference Ar cross section data set $\sigma_R(E)$ was compiled from benchmark measurements.[7] By employing a heated nozzle (60–100 °C) and using low backing pressure (15–20 psi), little evidence of clustering was observed in the EI mass spectra. The sample delivery lines and pulsed valve interior were passivated by the flow of sample through the valve requiring a few hours of operation before stable hydrazine mass spectra were observed.

The present method eliminates many of the shortcomings of more conventional techniques as discussed elsewhere.[7] Problems with ion extraction efficiency are avoided by using pulsed extraction (100 V, 4 μs) and acceleration (1500 V) after field-free ionization. TOF mass spectrometry permits simultaneous detection of more than one ion mass signal making the intensity ratio measurement in Eq. (1) very reliable. The need to fully characterize the electron beam properties (flux, divergence, interaction length, dependence on energy) is therefore eliminated. The only m/z dependent instrumental effects of significance in our experiment are due to deflection voltage, MCP detector gain, and lack of uniformity of the relative number density n_R/n_M in the molecular beam. We express the instrument

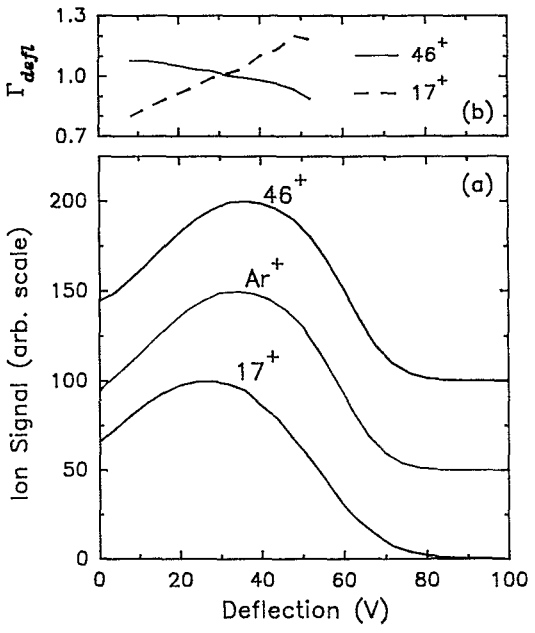

FIG. 3. (a) Ion signal vs deflection voltage for Ar^+ and MMH ionization fragment masses 46 and 17. All curves are normalized to a 0–100 scale and offset by 50 units for clarity. (b) The intensity ratio f^R_{defl}/f^M_{defl} where $R=Ar^+$ and $M=46^+$, 17^+, constitutes the correction factor Γ_{defl} in Eq. (2). Normally ion signals are measured relative to a reference ion of similar mass (e.g., 17^+ and Ne^+)

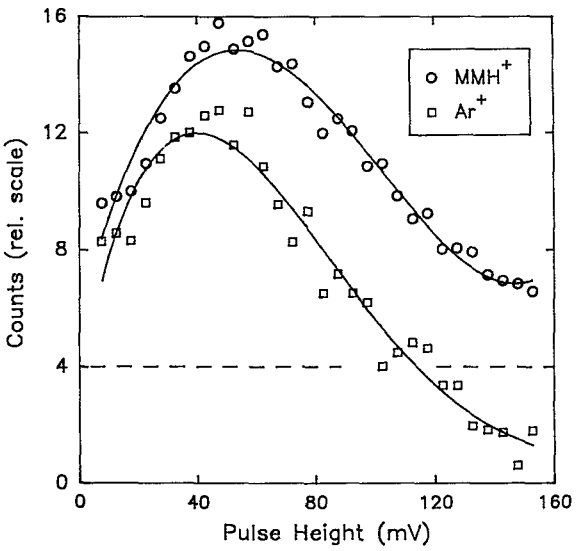

FIG. 4. Pulse height distributions for detection of Ar^+ and MMH^+ produced by 170 eV excitation. The MMH^+ curve is offset; the dashed line is the baseline. Measurements are for amplified and filtered ion pulse shapes (see the text). Counts were measured over 5 mV channels. Both sets of results were normalized to the same total counts. Curves are drawn through points for clarity.

function $\kappa_{M,R}$ in Eq. (1) in terms of these three contributions, respectively, by

$$\kappa_{M,R}=\Gamma_{defl}\Gamma_{det}\Gamma_{nrel} \tag{2}$$

which we discuss below.

Deflection term. Deflector plates are used to compensate for the velocity of the atomic beam, which is perpendicular to the field that accelerates the ions toward the detector (Fig. 1). The deflection efficiency is measured by recording ion intensity vs deflection voltage. The deflection response varies with m/z as seen in Fig. 3(a). However, because the ions studied in this work do not encompass a large mass range ($m/z \leqslant 46$ amu), the maximum ion signal occurs at nearly the same deflection voltage. The Γ_{defl} values in Fig. 3(b) are obtained from the ratio of deflection efficiencies f^R_{defl}/f^M_{defl} from Fig. 3(a) (where f is the fraction of the maximum intensity). The maximum correction factor Γ_{defl} applied to any measurement was 16%; the overall uncertainty in signal intensity due to the deflection term is believed to be less than 5%.

Detector gain. The gain of an electron multiplier detector varies with the mass and velocity of the impacting ion, which introduces an m/z discrimination effect.[32,33] Pulse counting is less affected by this problem and for this reason is used in these experiments to record relative cross sections for different ions for scaling the energy-dependence ion yield curves. (In fact, there was very little difference in the relative cross sections measured by current and counting modes for the singly charged ions). However, m/z effects can also corrupt pulse counting measurements because pulse height distributions depend on gain, which can vary for different ions. This is a particular problem for ions of different charge, because they are accelerated into the detector surface with much different impact energies.[7] Far less variation in gain is observed for ions of the same charge. However, it is known that detector gain can be greater for molecular ions than for atomic ions of similar mass, an effect also observed here.[33] In Fig. 4, the pulse height distribution for MMH^+ shows a response that is shifted to larger pulse heights relative to Ar^+, corresponding to an increase in average gain of 13%. Presumably, molecular ions break apart upon impact and the resulting fragments can potentially eject more primary electrons from the detector surface. We use a sufficiently low discriminator level (10 mV) for ion counting to avoid counting error due to varying pulse height distributions.

Relative density of sample and reference. The validity of using Eq. (1) to obtain absolute cross sections depends on the premixed ratio n_R/n_M remaining uniform in the molecular beam expansion. The correction factor Γ_{nrel} represents the ratio of n_R/n_M in the premixed sample to that in the molecular beam at the excitation region. The value Γ_{nrel} is likely to deviate from unity because of the dependence of the radial velocity in the supersonic expansion on mass.[34] This effect, which causes an increased concentration of heavier masses along the beam centerline (i.e., mass focusing), was evident in a previous experiment comparing cross sections measured for Kr and Xe [referenced to Ar, Eq. (1)] to literature values. The measured cross sections exceeded the known values by roughly 5%–10% for Kr and 10%–15% for Xe by assuming $\Gamma_{nrel}=1$. In the present experiment, Γ_{nrel} deviates much less from unity because the target ions are all relatively light and are referenced to an internal calibrant rare gas atom of similar mass. We there-

fore assume $\Gamma_{nrel}=1$, which we estimate to be correct to within 5% for all cases reported here. Mass focusing does not affect the shape of the cross section curves with energy.

The uncertainties in the measured cross section values are stated as follows. The total cross sections are estimated to be accurate to $\pm 10\%$. The measured fragment-ion cross sections are affected by the kinetic-energy detection efficiency of our apparatus as described in the following section. The majority of ions are detected at near unit collection efficiency relative to a rare-gas or parent-ion reference signal. These cross sections are reported to about $\pm 10\%$–15% accuracy. The uncertainty increases with increasing fragment ion KE. A detection efficiency for all ions is determined from the measured KE distributions, which can be used to correct the raw cross section values. However, this correction is approximate which means that the accuracy of the reported cross sections of the most energetic ions is no better than $\pm 50\%$.

C. Kinetic-energy analysis

Velocity distribution. The kinetic energy (KE) of fragment ions appears as an observable and interpretable quantity in two measurements: the shape of ion deflection curves[35] [e.g., Fig. 3(a)] and the shape of ion TOF peaks.[35–38] For randomly distributed velocity vectors, the 3D laboratory-frame velocity probability in velocity space is given by the product of the component probabilities

$$P(v)dv=\prod_{i=x,y,z} P(v_i)dv_i\,. \tag{3}$$

Fragment ion $P(v)$ distributions are determined directly from the data, however, for this discussion it is convenient to consider a Gaussian function, which fits well to the majority of experimental results. A normalized Gaussian probability function of width σ for the velocity component along a single axis is given by

$$P(v_i)dv_i=\left(\frac{1}{\pi\sigma^2}\right)^{1/2}\exp\left(-\frac{v_i^2}{\sigma^2}\right). \tag{4}$$

The velocity distribution for fragment ions recoiling from a common origin can be viewed as an expanding sphere. Equations (3) and (4) describe the probability of finding in a volume element $dv_x\,dv_y\,dv_z$ a particle with a velocity component between v_x and v_x+dv_x, and so forth for y and z. The 3D laboratory-frame velocity or speed is related to the component velocities by the relation $v^2=v_x^2+v_y^2+v_z^2$.[39]

The ion-deflection and TOF methods for measuring KE distributions are based on the principle of measuring a single velocity-component probability function $P(v_i)dv_i$. The ion deflection technique is illustrated in Fig. 5. The expanding ion velocity sphere (ion packet) is deflected across the detector which in effect integrates $P(v)$ along a single coordinate. If we assume that the diameter of the ion packet is smaller than that of the detector and that the detector edge is straight (i.e., the limit of very large detector), then the deflection function represents a running integration along z and a full integration over x and y. The measured curve $\Phi(v_z)$ is described by the function

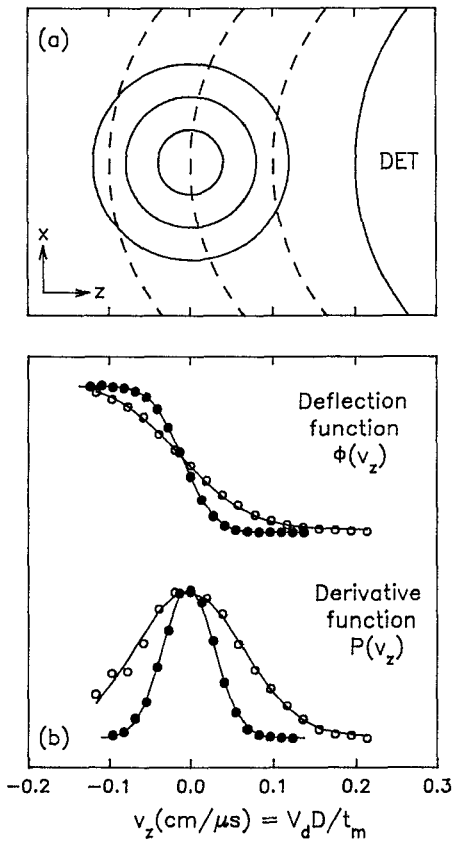

FIG. 5. Method for measuring KE distributions by the ion deflection method. (a) Pictorial of the ion packet velocity contours in the plane of the detector (DET) face. (b) Observed differential $P(v_z)$ and integral $\Phi(v_z)$ velocity probability functions and Gaussian fits for parent ion $N_2H_4^+$ (●) and fragment ion NH_2^+ (○). The $N_2H_4^+$ signal, which has no recoil KE, serves as the instrument function for deconvolution. The terms equated to v_z on the abscissa are described in the text.

$$\Phi(v_z)=\int_{-\infty}^{\infty}dv_x'\int_{-\infty}^{\infty}dv_y'\int_{-\infty}^{v_z}dv_z'\,P(v_z')P(v_y')P(v_x') \tag{5}$$

$$=\int_{-\infty}^{v_z}P(v_z')dv_z' \tag{6}$$

Measured and calculated (Gaussian) deflection curves $\Phi(v_z)$ are plotted in Fig. 5(b). The derivative of this response yields the z-component velocity probability

$$\frac{d\Phi(v_z)}{dv_z}=P(v_z). \tag{7}$$

The corresponding measured and calculated $P(v_z)$ curves are given in Fig. 5(b). The 3D velocity probability $P(v)$ is obtained by equating $P(v_x)$ and $P(v_y)$ to the measured probability $P(v_z)$ [Eq. (3), which assumes an isotropic distribution). The quantity of interest is the number density or fraction of molecules $f(v)$ with velocity between v and $v+dv$. This function, sometimes referred to as the speed distribution, represents the radial dependence of $P(v)$ and is obtained by converting to polar coordinates and integrating over the angular variables to give[39]

$$f(v)dv = P(v)4\pi v^2\, dv. \tag{8}$$

The same result is obtained by recognizing that the number density is a function of the velocity volume element $4\pi v^2\, dv$.

The measured deflection curves are recorded in coordinate space and the transformation to velocity space is obtained by the relation $v_z = z/t_m$, where t_m is the flight time for mass m. The coordinate z is related to the deflection voltage V_d by the relation $z = V_d D$, where D is a conversion factor relating ion packet displacement to change in deflection voltage (i.e., $D = \Delta z/\Delta V_d$). D is determined by recording the ΔV_d required to scan the ion packet across the known dimensions of the detector. The value of D varied only moderately (0.033–0.040 cm/V) for a variety of ion masses and carrier gases. KE distributions are plotted as $f(v)$ vs $mv^2/2$ and mean KE values $\langle \epsilon_t \rangle$ are obtained from the averaging expression

$$\langle \epsilon_t \rangle = m \sum v^2 f(v) \Delta v / 2 \sum f(v) \Delta v\,. \tag{9}$$

The TOF peak-shape method is similar to the ion-deflection method for measuring KE in that a single velocity-component probability function $P(v_i)$ is measured. The main difference between the two methods is that the TOF distribution is a time-resolved response that measures the differential function $P(v_i)$ directly. Also the velocity component that is measured is v_y, which is defined along the drift-tube axis. It is assumed here that the ion-packet size is small relative to the detector area so that $P(v_x)$ and $P(v_z)$ are fully integrated in the manner of Eq. (6). The TOF distributions arise because of the varying effect the extraction field $\mathscr{E}$ has on fragment ions of different velocity. Ions that have velocity components directed away from the detector are reversed by the field $\mathscr{E}$. The time Δt required to return the ions to their original position depends on v_y. The separation in time of ions impacting the detector is therefore a measure of initial ion velocity. Δt is determined by solving for the time that the ion velocity component under the influence of the field comes to a stop before heading toward the detector, i.e.,

$$v_y + \frac{q\mathscr{E} t}{m} = 0 \tag{10}$$

which leads to the expression

$$v_y = \frac{q\mathscr{E}\Delta t}{2m}\,. \tag{11}$$

The distribution of v_y values creates a distribution of arrival times. For a Gaussian TOF peak shape, the temporal width is transformed to a velocity width σ using Eq. (11). It is straightforward to show that the Gaussian width σ [Eq. (4)] is related to the mean velocity $\langle v \rangle = \int v f(v) dv / \int f(v) dv$ by the relation $\sigma = (2/3)^{1/2}\langle v \rangle$. Values of $\langle \epsilon_t \rangle$ are obtained from TOF analysis by the expression

$$\langle \epsilon_t \rangle = \frac{m\langle v^2 \rangle}{2} = \frac{3m\sigma^2}{4}\,. \tag{12}$$

It is worth noting that the TOF peak shape and deflection analysis probe different velocity components. In principle, a series of TOF measurements as a function of deflection voltage could be used to map out a 2D image of the fragment ion KE distribution, which would be of interest if the KE distribution were anisotropic. In this case, it is preferable to have a detector size that is small relative to the ion-packet size to avoid averaging over orthogonal velocity components. We are working to implement 2D KE determinations to obtain absolute differential (angle-velocity resolved) cross sections for dissociative ionization.

Deconvolution. The size of the initially formed ion packet ($\simeq$0.5 cm diam.) causes broadening in the deflection curves that erodes resolution (Fig. 5). Response functions are obtained by recording deflection curves of a rare gas ion or a parent ion, since they have no kinetic energy other than initial thermal energy (which is negligible in the molecular beam). The derivative curve of the response function g and the observed signal function s are well described by Gaussian functions as shown in Fig. 5(b). This greatly simplifies the deconvolution leading to the actual function p. It is straightforward to show from the convolution equation

$$s(x) = \int_{-\infty}^{\infty} p(u) g(x-u)\, du \tag{13}$$

and the convolution theorem of Fourier transforms[40]

$$\mathscr{F}\{s\} = \mathscr{F}\{p\}\mathscr{F}\{g\}, \tag{14a}$$

$$p(u) = \mathscr{F}^{-1}\left[\frac{\mathscr{F}\{s\}}{\mathscr{F}\{g\}}\right] \tag{14b}$$

that the deconvolved function p is a Gaussian of width $\sigma = [\sigma_s^2 - \sigma_g^2]^{1/2}$, where σ_s and σ_g are the widths of functions s and g, respectively. Deconvolution is achieved by simply rescaling the v_z data array of s by the factor σ/σ_s.

Kinetic-energy detection efficiency. It is necessary to consider the detection efficiency of fragment ions of varying KE because it affects the accuracy of measuring fragment ion cross sections and KE distributions. Ideally, the detector diameter should greatly exceed the ion-packet dimensions. For KE measurements one might alternatively choose a very small detector size in order to directly measure a single velocity-component distribution without making the assumption in Eq. (6) of averaging over all other components. The finite size of the detector means that the limits of integration over dv_x' and dv_y' in Eq. (6) are also finite. The upper limit of integration imposed by the detector varies with mass in velocity space, but is a constant in energy space. For cross section measurements, the x and y components of the ion packet will be truncated by the size of the detector, but the y component is fully detected (cf. Fig. 5). If we assume Gaussian velocity-component probability functions [Eq. (4)], then the detector efficiency is equal to $[\mathrm{erf}(x)]^2$, [where $\mathrm{erf}(x) \equiv \pi^{-1/2}\int_{-x}^{x} \exp\{-a^2\}\, da$] and $x = r/t_m\sigma$, r is the detector radius (0.9 cm), and t_m is the ion-mass time of flight. The latter value is given by $t_m = l(m/2U)^{1/2}$, where l is the drift tube length (100 cm) and U is the ion energy after acceleration (1550 eV). Using

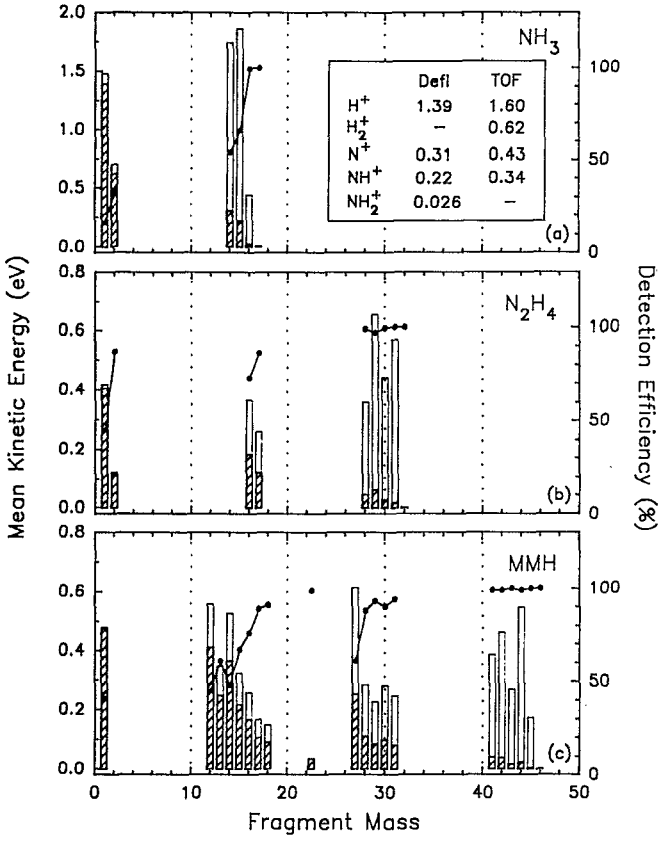

FIG. 6. Mean fragment kinetic energy $\langle \epsilon_t \rangle$ and center-of-mass kinetic energy $\langle \epsilon_t \rangle_{c.m.}$ for 170 eV excitation are represented by the height of the cross-hatched and open bars, respectively. The latter set of values assumes two-body dissociation (cf. Ref. 49), although some fragments are best described by sequential multibody dissociation mechanisms, as discussed in the text. The data point at 22.5 is due to doubly charged mass 45 and has a value of $\langle \epsilon_t \rangle_{c.m.} = 1.8$ eV. The insert compares values of $\langle \epsilon_t \rangle$ for NH_3 ionization measured by the deflection and the TOF methods. The solid dots and lines are detection efficiencies and refer to the scale on the right hand side.

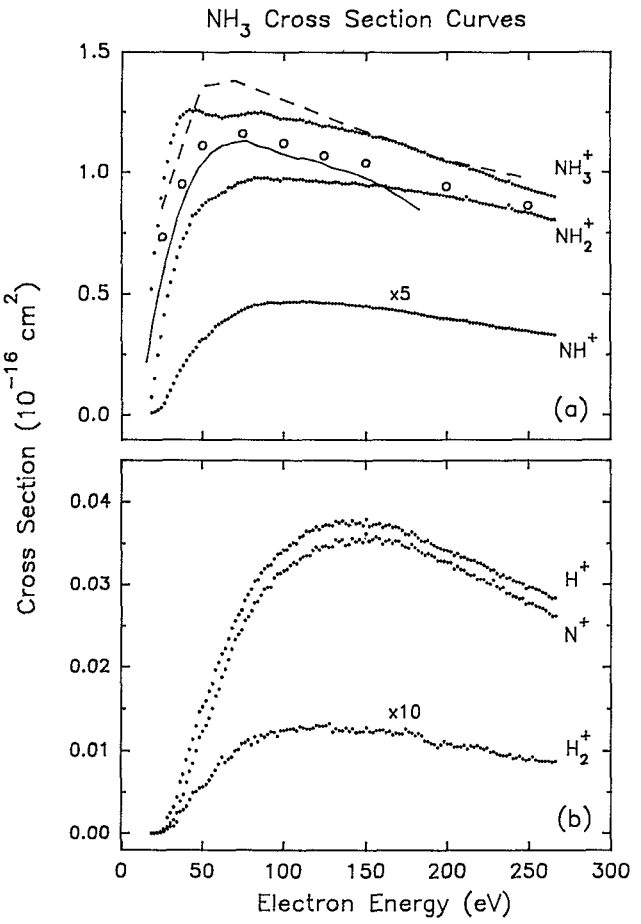

FIG. 8. Partial dissociative-ionization cross sections for NH_3 as a function of electron energy. NH_3^+ data from other studies are given above and identified in the legends and caption to Fig. 7. Cross sections have not been corrected for KE detection efficiencies reported in Fig. 6(a).

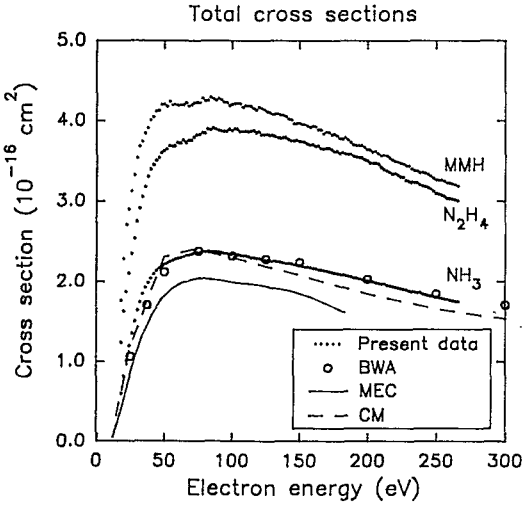

FIG. 7. Total EI cross sections for NH_3, N_2H_4, and MMH as a function of electron energy. The NH_3 data of BWA (Ref. 16), MEC (Ref. 17), and CM (Ref. 18) are included for comparison.

Eq. (12) it follows that $x=[0.19/\langle \epsilon_t \rangle]^{1/2}$ (eV units). The $\langle \epsilon_t \rangle$ values and detection efficiencies for all ions studied are tabulated in Fig. 6. The use of a shorter drift tube length l in future experiments will significantly improve the KE detection efficiency since the KE detection limit is proportional to $U(r/l)^2$.

Caveats. Deflection curves were recorded for the purpose of measuring relative detection efficiencies for different ion masses (Sec. II B, Fig. 3) and only after the experimental phase of this work was completed did it become apparent that KE information could be obtained from these data. Several refinements are being implemented for future measurements. The present KE measurements are preliminary data that are important for assessing the accuracy of measured cross sections for energetic fragments and for interpreting fragment dissociation mechanisms (Sec. IV B). They are not of sufficient accuracy for determining dynamical properties of dissociation (i.e., energy partitioning, energy-redistribution rates, dissociation rates). The measurements are fair in terms of resolution and absolute energy (about ±20%–50%), but good in terms of uniform detection efficiency with KE (allowing

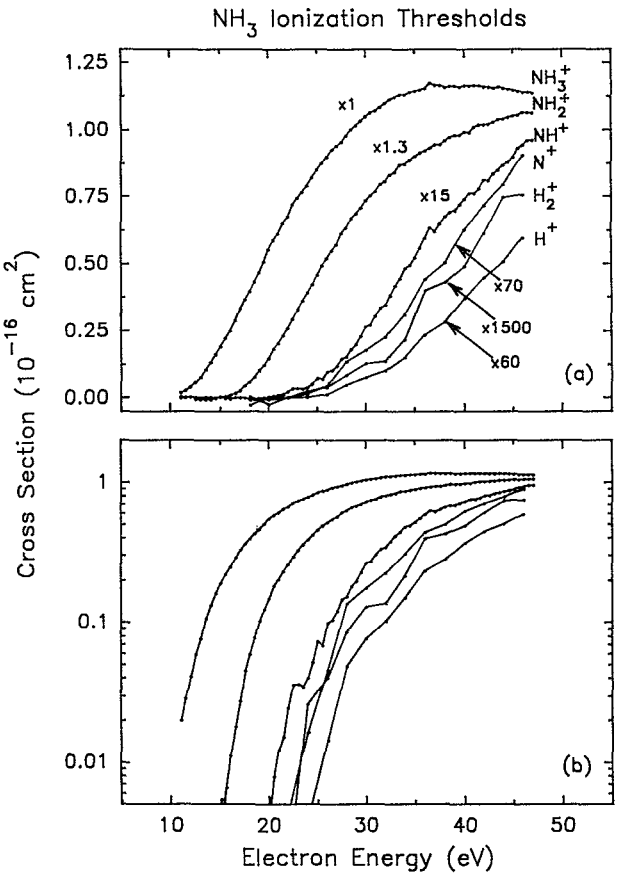

FIG. 9. Dissociative-ionization cross sections for NH_3 recorded at higher resolution in the threshold region. (a) and (b) are linear and log σ scales, respectively.

$\langle \epsilon_t \rangle$ determinations) and for relative KE comparisons for different fragments (about $\pm 10\%$–20%).

III. RESULTS AND ANALYSIS

A. NH_3 results

1. Dissociative-ionization cross sections

The total ionization cross sections for NH_3, N_2H_4, and MMH, are plotted in Fig. 7. The results of Bederski, Wójcik, and Adamczyk (BWA),[16] Märk, Egger, and Cheret (MEC),[17] and Crowe and McConkey (CM)[18] for NH_3 are included for comparison. The cross section measured in this work at 70 eV (2.35 Å^2) compares reasonably well with the values reported by BWA (2.3 Å^2), MEC (2.02 Å^2), and CM (2.4 Å^2). The cross section curves show noticeable, but not serious differences. Partial cross sections for production of parent and fragment ions are given in Figs. 8 and 9 (the latter figure was recorded at higher resolution to emphasize the threshold region). The reported cross sections are uncorrected for the dependence of detection efficiency on KE. Corrections are appropriate only for the highest energy fragments. Detection efficiencies for all fragments are reported in Fig. 6.

NH_3^+ *parent ion.* The NH_3^+ parent ion curve is compared to the data of BWA,[16] MEC,[17] and CM.[18] A structured curve is evident in the present results with peaks occurring at about 42 and 86 eV. BWA, MEC, and CM observed a single peak at about 75, 75, and 65 eV, respectively. The failure to observe structure in these previous studies may be a result of using too large an energy increment, or it may indicate an artifact in the present data. However, there are several arguments against the latter possibility. First, we always record ionization curves for three ions simultaneously (e.g., Ar^+, NH_3^+, and a fragment ion). Yet the structure is only noticeable for NH_3^+ and not for the fragment curves. The simultaneous measurement of the calibrant Ar^+ signal also eliminates errors due to changes in electron beam current. Second, the structure was also observed in an earlier study that used a prototype version of the current technique.[9] So it is not a peculiarity of a particular set of conditions. Third, similar structure is observed for N_2H_4 and MMH, although, there are significant differences that would argue against a common artifact. Finally, no such structure was observed for an extensive series of measurements of multiple ionization of rare gases (Ar^{n+}, Kr^{n+}, and Xe^{n+}, $n=2$–6).[7]

NH_2^+ *and* NH^+ *fragment ions.* The relative cross sections for dissociative ionization measured in this work are compared to previous measurements in Table I. There is good agreement for NH_2^+ among the work of BWA,[16] MEC,[17] CM,[18] and here. There is substantial disagreement, however, for NH^+. Our cross sections are about a factor of two *larger* than MEC and about a factor of three *smaller* than CM, but comparable to BWA (30% larger after correcting for KE detection efficiency, below). Measurements by Gomet[19] and Melton[20] are also in reasonable agreement with the present data. It is apparent from the KE distributions in Figs. 10 and 11 [also Fig. 6(a)] that the NH^+ fragment is formed with a relatively large amount of kinetic energy ϵ_t. The analysis described in Sec. III A 3 leads to a value of $\langle \epsilon_t \rangle \simeq 0.22$ eV for NH^+, which we compare to the value of $\langle \epsilon_t \rangle < 0.03$ eV for NH_2^+ (measured at 170 eV). CM concede that their apparatus "tends to overestimate the contribution of energetic fragment ions" and for this reason caution that these cross sections may be high. The apparatus of MEC, on the other hand, uses low extraction fields and small detection apertures that can discriminate against energetic fragments ions and cause a low cross section reading. Our experiment is less sensitive to KE discrimination and more importantly, the detection efficiency is known, which for NH^+ is 0.68 (Fig. 6).

N^+ *and* H^+ *fragment ions.* The comparison of cross section values in Table I shows substantial discrepancy among different studies for the N^+ and H^+ ions. Our values are much smaller than those of BWA[16] and considerably larger than those of MEC.[17] CM did not report measurements of these ions.[18] The KE measurements reported in Figs. 6(a) and 11 indicate significant kinetic-energy releases for N^+ and H^+, which may explain the low values of MEC. Our measurements also suffer from KE discrimination, but can be corrected using the detection efficiencies reported in Fig. 6(a). This brings the N^+ cross section in line with BWA, but causes the H^+ value to exceed the BWA value. Finally, we note that the very similar shape of

TABLE I. Ratios of partial cross sections for NH_3 dissociative ionization.

		$\sigma(M^+)/\sigma(NH_3^+)$				
M^+	E(eV)	This work[g]	BWA[a]	MEC[b]	C.M.[c]	Other
NH_2^+	50	0.70	0.80	0.70	0.71	
	100	0.79	0.90	0.80(0.83)	0.79	
	150	0.82	0.93	0.84	0.78	
	200	0.86	0.96	···	0.78	
NH^+	50	0.050	0.069	0.025	0.18	
	100	0.076	0.086	0.030(0.055)	0.24	
	150	0.077	0.087	0.030	0.24	
	200	0.076	0.082	···	0.23	
N^+	50	0.009 7	0.021	0.006	···	0.006[d]
	100	0.026	0.039	0.011(0.019)	···	0.016[d], 0.03[e], 0.017[f]
	150	0.031	0.044	0.012	···	0.009[d]
	200	0.031	0.043	···		···
H_2^+	50	0.000 43	0.0021	0.002	···	0.009[d]
	100	0.001 00	0.0021	0.002	···	0.002[d], 0.026[e], 0.0002[f]
	150	0.001 06	0.0022	0.002	···	0.0012[d]
	200	0.001 02	0.0020	···		···
H^+	50	0.012	0.043	0.007	···	0.086[d]
	100	0.028	0.066	0.011	···	0.085[d], 0.026[e], 0.005[f]
	150	0.032	0.071	0.011	···	0.023[d]
	200	0.032	0.071	···		···

[a]Reference 16.
[b]Reference 17. 50 and 150 eV values are actually for 47.7 and 150.5 eV. The values in parentheses were obtained using a higher electron beam current.
[c]Reference 18.
[d]Reference 19.
[e]Reference 20.
[f]Reference 21.
[g]Data are not corrected for the KE detection efficiencies reported in Fig. 6(a).

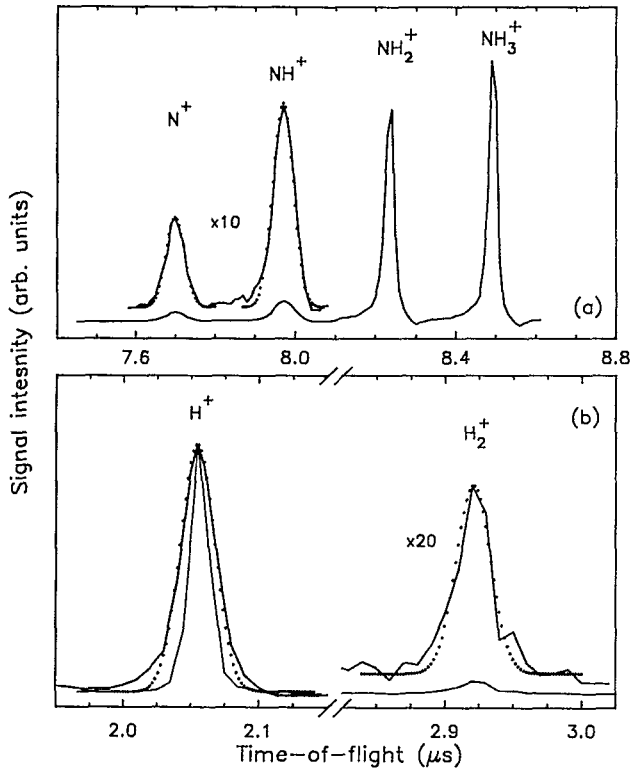

FIG. 10. TOF peak shapes and intensities and calculated kinetic-energy distributions for 170 eV NH_3 dissociative ionization. (a) NH_3^+ and fragments NH_2^+, NH^+, and N^+; (b) fragments H_2^+ and H^+. The zero kinetic energy He^+ peak shape is superimposed on the H^+ peak for comparison. The He^+ signal is used to deconvolve the H^+ and H_2^+ peak shapes and the NH_3^+ signal is used to deconvolve the N^+ and NH^+ peak shapes to obtain the Gaussian velocity width σ. Eq. (12) leads to $\langle \epsilon_t \rangle$ values 1.6, 0.62, 0.43, and 0.34 eV for H^+, H_2^+, N^+, and NH^+, respectively.

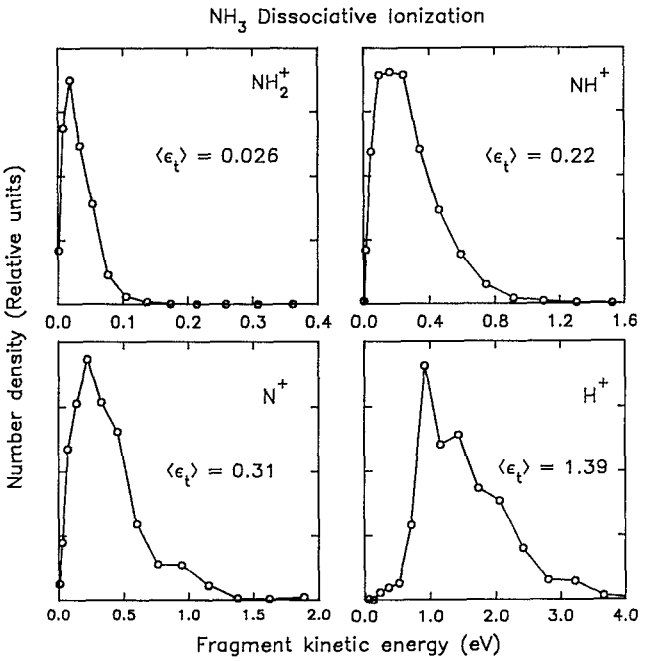

FIG. 11. Fragment KE distributions determined by the deflection technique for 170 eV NH_3 dissociative ionization. Note different energy scales. Apparent structure may not be real. The $\langle \epsilon_t \rangle$ values are determined using Eq. (9).

TABLE II. Thermochemical thresholds and appearance potentials for dissociative ionization of NH_3.

		Electron impact			Photoionization	
Products	ΔH(eV)[a]	This work	Ref. 22	Ref. 17	Ref. 10	Ref. 11
$NH_2^+ + H$	15.77	15.5	15.76	16.5	15.71	16
$NH^+ + H_2$	17.55	20	16.9,18.0		18.23	20
$+2H$	22.06		22.6	22.9	22.75	
				27.2		
$N^+ + H + H_2$	22.03	22.5	22.5			
$+3H$	26.55			29.5	26.05	28
$H_2^+ + NH$[b]	19.48			14.8		
$+N+H$	22.91	23	22.3,26.6		25.62	
$H^+ + NH_2$	18.23		19.5			
$+N+H_2$	21.08					
$+H+NH$[b]	22.17	24	22.6	23.0	23.57	23
$+N+2H$	25.60		26.2	27.7	25.62	
				30.6		

[a]Values are from Ref. 10.
[b]Thresholds corresponding to the NH electronic states $X\,^3\Sigma$, $a\,^1\Delta$, $b\,^1\Sigma$, $A\,^3\Pi$, and $c\,^1\Pi$ occur at 0, 1.58, 2.63, 3.69, and 5.40 eV higher energy, respectively.

the H^+ and N^+ curves may be a result of a Coulomb repulsion of NH_3^{2+}.

H_2^+ *fragment ions.* H_2^+ is the least abundant of the fragments reported here, having a signal strength about 3% that of H^+ (Figs. 8–10). A huge variation exists in the cross sections for this fragment reported by different studies. The values of MEC are larger than reported here, which is opposite to the trend of undermeasuring the cross sections of energetic fragments H^+, N^+, and NH^+ (Table I). Curiously, the appearance potential of 14.8 ± 0.2 eV reported by MEC is much less than the lowest thermochemical threshold of 19.5 eV (Table II, Sec. III C). Other groups reporting low threshold values for H_2^+ are Mann *et al.* (15.5 ± 0.5 eV)[21] and Locht *et al.* (15.5 ± 0.2).[22] The latter group determined that this source of H_2^+ arises from neutral H_2 (IP = 15.5 eV) most likely produced by thermolysis of NH_3 on the hot filament in the ion source. BWA also reports cross sections that are about twice as large as here, however, the resolution in the threshold region is not sufficient in their study to determine whether a H_2 impurity is contributing to their signal. Contamination caused by decomposition on surfaces is avoided in the present work by using a molecular beam sample.

2. Thermochemical and excited state thresholds

Several previous measurements of ion fragment appearance potentials have been reported for EI[17,22,23] and PI[10–12] of NH_3. The more extensive of these studies are summarized and compared with our results in Table II. We have reported our appearance potentials to the nearest 0.5 eV, which represents the limit of our resolution. There is considerable discrepancy among the results compiled in Table II (often exceeding each experimenter's quoted error limits). The case for H_2^+ was already discussed above. Our data are consistent with thermochemical thresholds and the concensus of experimental data. This comparison is important for validating our measurements for the hydrazines for which little data exists on fragmentation thresholds.

The ground electronic state of NH_3 is a pyramidal structure of C_{3v} symmetry and that of NH_3^+ ion is planar D_{3h}, corresponding to removal of a lone-pair nonbinding electron.[41] The electronic configurations for the ground states of NH_3 and NH_3^+ are given below along with the molecular orbital (MO) vertical and adiabatic ionization potentials of NH_3 (in eV units)

$$[1a_1]^2_{1sN}[2a_1]^2_{2sN}[1e]^4_{\sigma_{NH}}[3a_1]^2_{2pN} \quad C_{3v}{:}\tilde{X}\,^1A_1(NH_3),$$

$$[1a_1']^2_{1sN}[2a_1']^2_{2sN}[e']^4_{\sigma_{NH}}[a_2'']^1_{2pN} \quad D_{3h}{:}\tilde{X}\,^2A_2''(NH_3^+),$$

$$\text{vIP} \quad [405.6][27.8][16.0][10.88] \quad \text{Refs. 41,42,}$$

$$\text{aIP} \quad [405.6][26][14.7][10.18] \quad \text{Refs. 43,44.} \quad (15)$$

The $2a_1$ orbital has some $1sH$ character and, therefore, contributes to bonding.[45] The $3a_1$ orbital is the nitrogen $2p$ nonbonding (lone-pair) orbital.

All ion fragment thresholds from NH_3 ionization occur above the aIP for the first excited state $\tilde{A}\,^2E'(1e^{-1})$. (Our symmetry labeling is for loss of a C_{3v} electron to form a D_{2h} electronic state.) Wight *et al.* reports that the ground state $\tilde{X}\,^2A_2''(3a_1^{-1})$ gives only NH_3^+ and that all fragment ions originate through excited states.[11] This conclusion is interesting because several fragment ion thresholds for the hydrazines lie below the first excited state (Sec. III B 2). Locht *et al.*[22] and Wight *et al.*[11] assign the first excited state $\tilde{A}\,^2E'(1e^{-1})$ as the major source of NH_2^+, perhaps because the NH_2^+ fragment threshold coincides closely with the broad photoelectron peak for this state. It is believed that this state does not directly dissociate, but rather

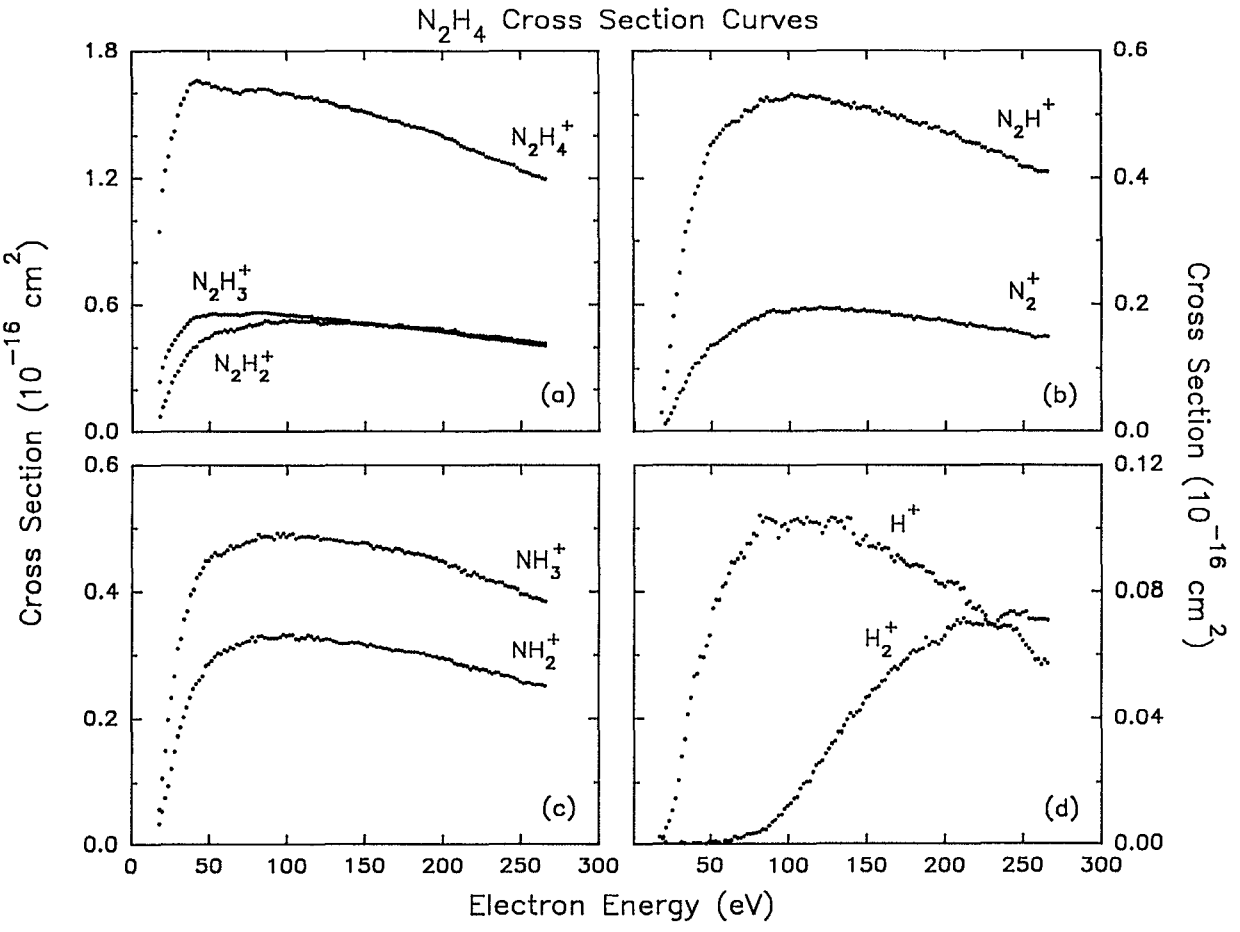

FIG. 12. Partial dissociative-ionization cross sections for N_2H_4 as a function of electron energy. Cross sections have not been corrected for KE detection efficiencies reported in Fig. 6(b).

undergoes a rapid internal conversion to the ground $\tilde{X}\,^2A_2''$, which correlates with H atom dissociation. The degenerate $\tilde{A}\,^2E$ state is split by Jahn–Teller interaction which produces a $^2A''$ component (in C_s symmetry due to a stretched N–H bond) that undergoes a conical intersection with the $\tilde{X}\,^2A_2''$ ground state.[46]

Wight *et al.* reports that the $\tilde{B}\,^2A_1'(2a_1^{-1})$ state accounts for virtually all the NH^+, N^+, and H^+ fragments (H_2^+ was not studied).[11] Locht *et al.* concurs, though he finds weak thresholds for NH^+ and H^+ attributable to the $\tilde{A}\,^2E'(1e^{-1})$ state.[22] The thresholds measured here and by Locht *et al.*, however, all occur below the broad photoelectron onset of 26 eV for $\tilde{B}\,^2A_1'(2a_1^{-1})$. This has led Locht *et al.* to propose the involvement of Rydberg states that converge to the $\tilde{B}\,^2A_1'(2a_1^{-1})$, but which autoionize to lower-energy ion states.

3. Fragment kinetic-energy distributions

KE analysis by the TOF and deflection methods are given in Figs. 10 and 11, respectively, and tabulated in Fig. 6. The deflection results were analyzed to obtain ϵ_t distributions, whereas the TOF results were used only to obtain a value $\langle\epsilon_t\rangle$ assuming a Gaussian velocity probability (Sec. II C). A summary of $\langle\epsilon_t\rangle$ values [insert in Fig. 6(a)] shows satisfactory agreement by both methods. The NH_2^+ and NH^+ velocity probabilities $P(v)$ leading to the ϵ_t plots in Fig. 11 [cf. Eq. (8)] are almost exactly Gaussian in shape (cf. Fig. 5). The N^+ velocity-probability curve deviates slightly from a Gaussian and the H^+ curve deviates much more so.

KE measurements for EI excitation of NH_3 were reported by Carnahan *et al.*[47] and Kurawaki and Ogawa[48] who measured excited state H atoms, and by Locht *et al.*[22] who measured ion fragments. The latter study is most relevant to this paper. These investigators achieved KE resolution sufficient to detect excited-state thresholds for fragment ions. However, the large thermal-energy component that peaks near-zero KE and the unknown collection efficiency as a function of KE makes it difficult to extract a mean value $\langle\epsilon_t\rangle$ for comparison with the present results. Figure 11 shows that NH^+ and N^+ are formed with similar energy and that NH_2^+ is formed with considerably less energy, in qualitative agreement with Locht *et al.*[22] The very large KE measured for H^+ is a result of the kinematics of momentum transfer for particles of different mass and not due to a large center-of-mass (c.m.) KE release [Fig. 6(a)].[49]

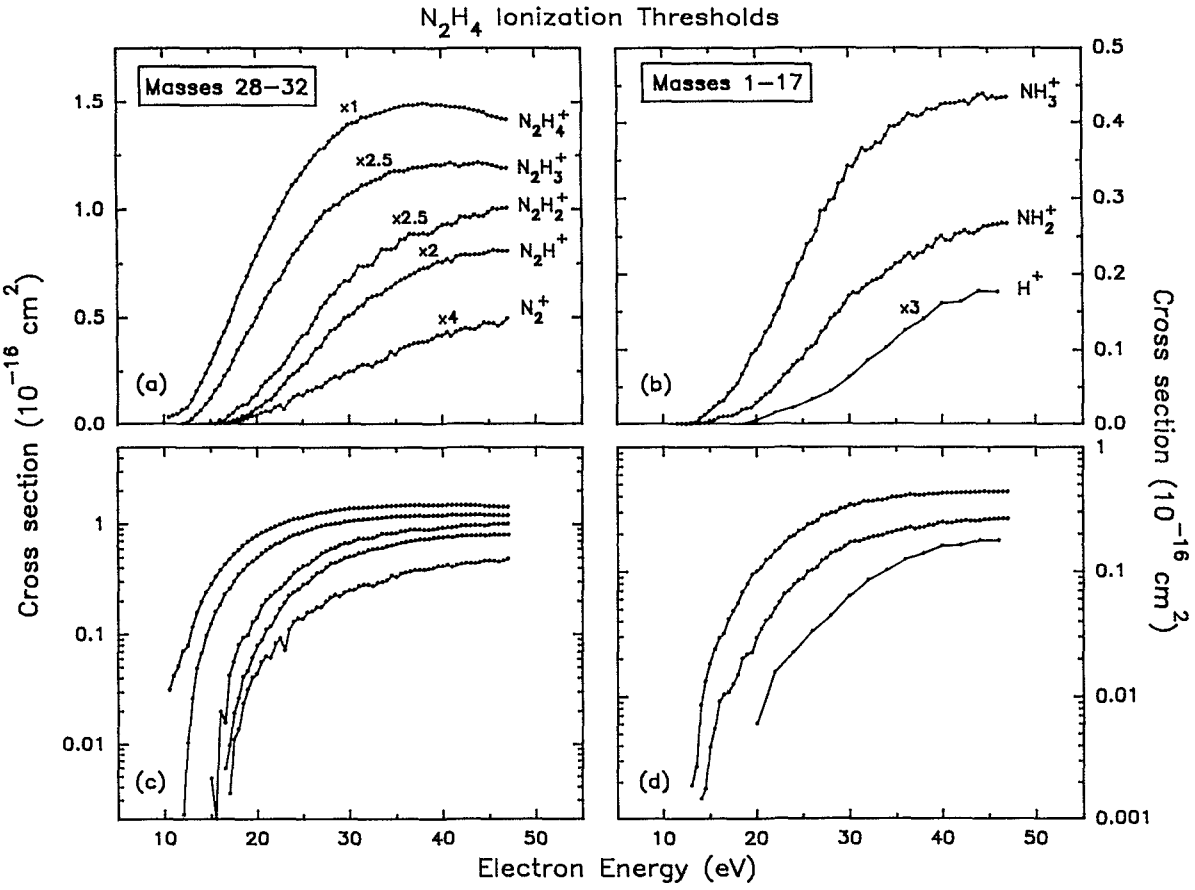

FIG. 13. Dissociative-ionization cross sections for N_2H_4 recorded at higher resolution in the threshold region. (a),(b) and (c),(d) are linear and log σ scales, respectively.

B. N_2H_4 results

1. Dissociative-ionization cross sections

The total ionization cross section curve for N_2H_4 in Fig. 7 is similar in shape to NH_3, but the magnitude is noticeably larger ($\sigma_{tot}=3.76$ Å^2 vs 2.35 Å^2, respectively at 70 eV). We are not aware of any previously measured cross sections for N_2H_4 ionization, however, the increase in magnitude relative to NH_3 is roughly proportional to the increase in the molecular area and number of electrons. Partial cross section curves are presented in Figs. 12 and 13; the latter figure shows the threshold region at higher resolution.

$N_2H_4^+$ *parent ion signal.* A structured cross section curve was observed for $N_2H_4^+$ resembling the structure observed for the parent NH_3 ionization signal in Fig. 8. The relative peak positions are nearly the same and for the reasons described earlier for NH_3^+, we have no reason to suspect any artifacts.

$N_2H_{4-n}^+$ $n=1$–4 *fragment ions.* The $N_2H_3^+$ cross section curve is similar in shape to the $N_2H_4^+$ curve including a correlation to the 40 eV peak. The curves for $N_2H_2^+$, N_2H^+, and N_2^+, which are similar as a group, differ from $N_2H_3^+$ in not showing an obvious relation to the 40 eV peak. Beyond 150 eV, all curves show similar behavior indicating that product branching ratios are nearly constant at these energies.

NH_3^+ *and* NH_2^+ *fragment ions.* The possibility that the strong NH_3^+ and NH_2^+ signals in Fig. 12(c) arises from an NH_3 impurity can be ruled out because the cross section curve for the fragment NH_3^+ has a different shape and threshold than the parent ion curve for NH_3^+ ionization [Fig. 8(a)] and because NH_3^+ is formed with significant KE [cf. Fig. 6(b) and below]. Furthermore, the shape of the NH_3^+ and NH_2^+ curves bear a strong resemblance to the $N_2H_{4-n}^+$ $n=2$–4 fragment ion curves, suggesting a common precursor. The presence of a species such as NH_3^+ and the nearly constant product branching ratios at higher energy indicate that the molecular ion undergoes extensive rearrangement prior to fragmentation (Sec. IV B).

H_2^+ *and* H^+ *fragment ions.* The propensity for producing H^+ is about the same for N_2H_4 and NH_3 ionization [$\sigma(H^+)/\sigma_{tot}$ is 0.025 (N_2H_4) vs 0.017 (NH_3) at 150 eV]. The properties of H_2^+ formation, though, are very different for the two molecules. The H_2^+ cross section curve for N_2H_4 ionization is unusual in that it has a rather high threshold of about 50 eV, yet it eventually reaches a relative cross section value much greater than that which oc-

TABLE III. Thermochemical thresholds and appearance potentials for dissociative ionization of N_2H_4.

Products	ΔH(eV)[a]	Electron impact: This work	Electron impact: Ref. 28	Photoionization: Refs. 24,25
$N_2H_3^+ + H$	11.10	12	11.3	11.11
$N_2H_2^+ + H_2$	10.52		11.9,10.75[b]	
$+2H$	15.03	15.5	16.6,15.25[b]	15.18
$N_2H^+ + H + H_2$	11.85		14.8	
$+3H$	16.36	16.5		
$N_2^+ + 2H_2$	14.45	17	16.2	
$+H_2+2H$	18.96			
$+4H$	23.47			
$NH_4^+ + N$	10.32			
$NH_3^+ + NH$	12.45	13		
$NH_2^+ + NH_2$	13.92	14.5		13.93
$NH^+ + NH_3$	15.79			15.70
$+NH_2+H$	20.30			
$N^+ + NH_3 + H$	20.09			
$+NH_2+H_2$	20.09			
$+NH_2+2H$	24.50			
$H_2^+ + N_2 + H_2$	14.29			
$+N_2H_2$	16.32			
$+N_2+2H$	18.80	50		
$H^+ + N_2 + H_2 + H$	16.99	18		
$+N_2H_3$	17.19			
$+N_2H_2+H$	19.10			

[a]Calculations by Pople and Curtiss (Ref. 57) for $N_2H_3^+$, $N_2H_2^+$, and N_2H^+. Remaining values were determined from heats of formation in Refs. 24, 25, and 58, and/or from thermodynamic cycles using thermochemical data in Refs. 24, 25, and 60.
[b]Reference 27.

curs for NH_3 ionization [$\sigma(H_2^+)/\sigma_{tot}$ is 0.021 (N_2H_4) vs 0.0044 (NH_3) at 250 eV]. The H^+ signal decreases with energy faster than the other fragment curves and with a slope that suggests a possible competition with H_2^+ formation.

2. Thermochemical and excited state thresholds

Dissociative-ionization cross sections for N_2H_4 in the threshold region are given in Fig. 13. The fragment thresholds measured here and in previous EI[27,28] and PI[24–26] experiments are compared to calculated thermochemical thresholds in Table III. Good agreement is obtained where previous data exist. New measurements are reported here for the fragments NH_3^+, H_2^+, and H^+. These values are consistent with the thermochemical thresholds.

The electronic structure and geometry of N_2H_4 and $N_2H_4^+$ are discussed in Paper I.[5] The geometry of the neutral ground state of N_2H_4 is of C_2 symmetry with pyramidal sp^3 nitrogen orbitals and a N–N dihedral angle of about 95° (*gauche*) with respect to the nonbonding orbitals.[50–52] This geometry is very unstable in the ground state ion, which has a planar D_{2h} geometry brought about by N–N bond rotation and rehybridization of the N orbitals to sp^2+p_π.[53,54] The electronic configurations of the neutral and ion ground electronic state are given below along with the molecular orbital IPs for N_2H_4

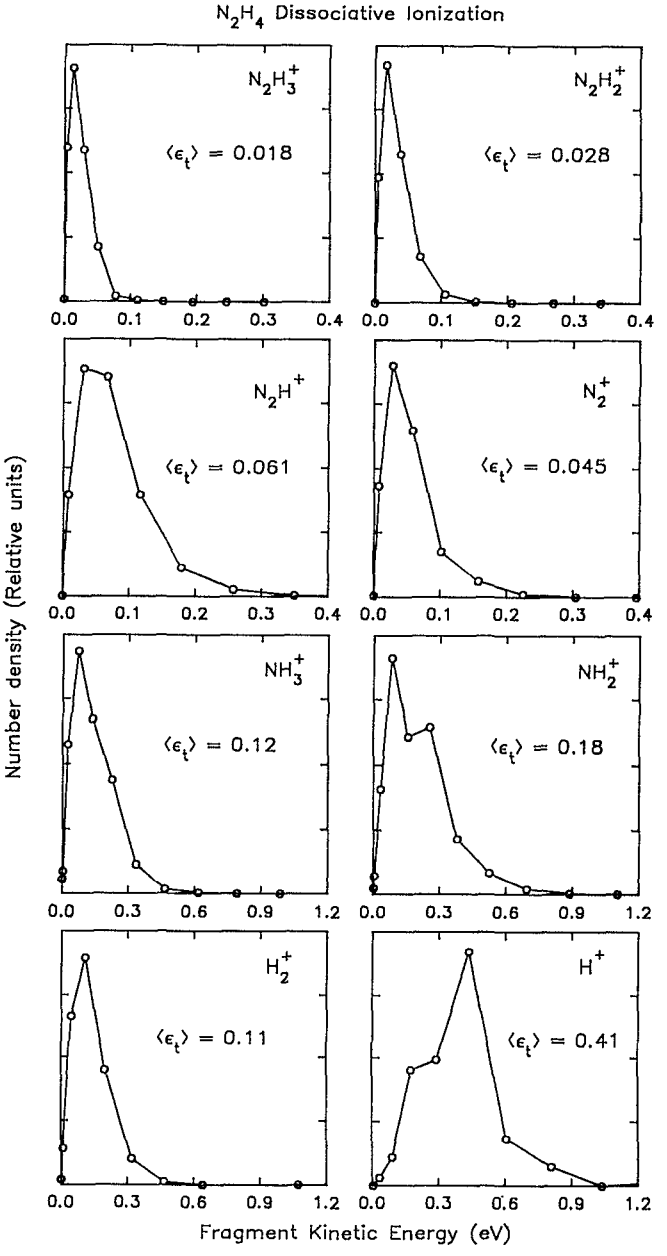

FIG. 14. Kinetic-energy distributions determined by the deflection technique for 170 eV N_2H_4 dissociative ionization. Upper four plots are on a 0.4 eV maximum scale and lower four plots are on a 1.2 eV maximum scale.

$$[1a^21b^2]_{1sN}[2a^2]_{\sigma_{NN}}[2b^23a^23b^24a^2]_{\sigma_{NH}} \times [4b^25a^2]_{n_\pm} \quad C_2{:}\tilde{X}\,{}^1A,$$

$$[1a_g^21b_{3u}^2]_{1sN}[2a_g^2]_{\sigma_{NN}}[2b_{3u}^21b_{1g}^21b_{2u}^23a_g^2]_{\sigma_{NH}} \times [1b_{1u}^21b_{2g}^1]_{\pi_\pm} \quad D_{2h}{:}\tilde{X}\,{}^2B_{2g},$$

vIP [420][~30][~25,16.8,16.7,15.6][10.64,9.91]
Refs. 29,55,

aIP [420][~30][~24,⋯,≤15.5,≤14.5][8.1,8.1]
Refs. 26,55,56. (16)

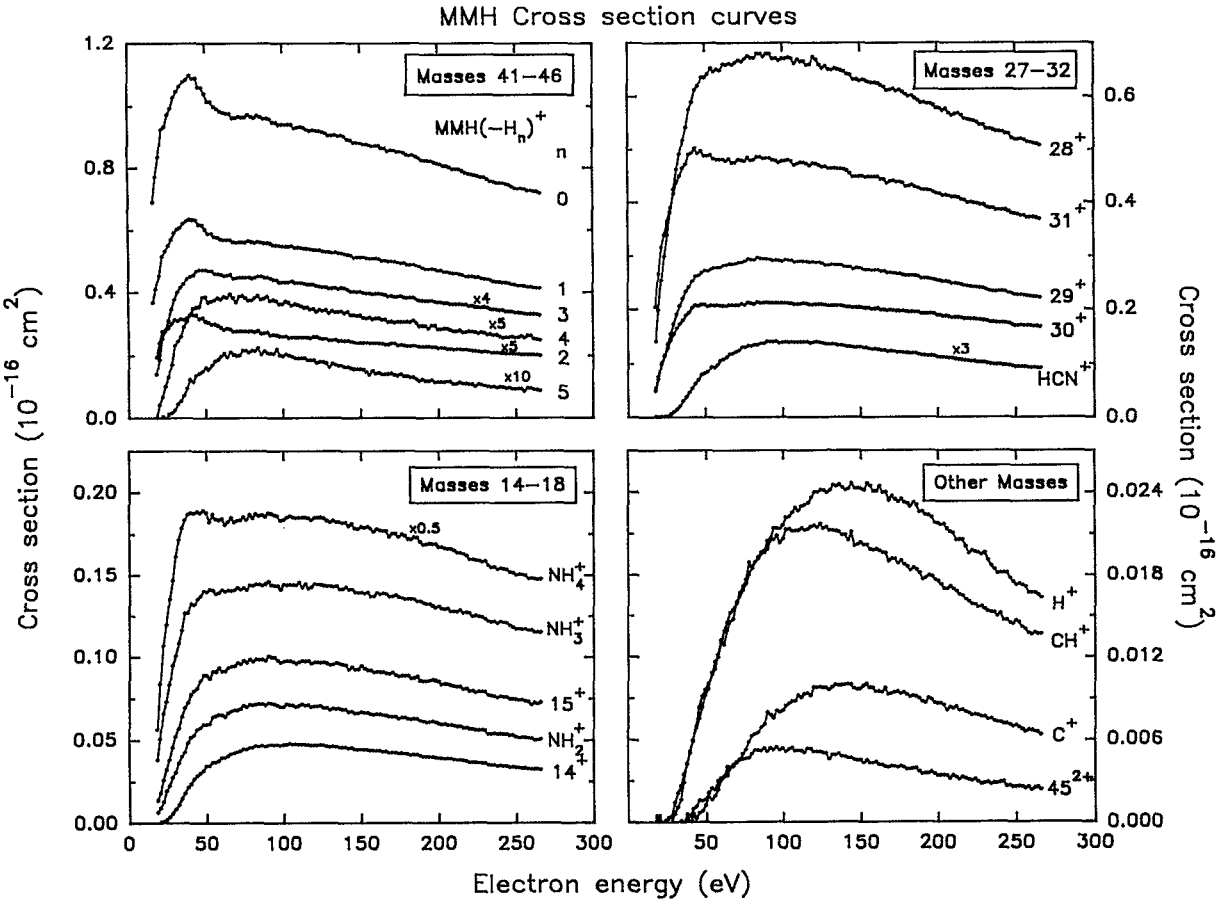

FIG. 15. Partial dissociative-ionization cross sections for MMH as a function of electron energy. MMH$(-H_n)^+$ designates loss of n number of H atoms. Cross sections have not been corrected for KE detection efficiencies reported in Fig. 6(c).

The axis system is defined such that z is the out-of-plane C_2 symmetry rotation axis and x and y are the long (N–N) and short axis in the molecular plane. The sequence of orbitals for C_2 are in order of calculated energies.[55] The quoted energies are a compilation of experimental and theoretical references. The energy ordering of the orbitals changes in going to D_{2h}; however, we list the orbitals in the same order as the C_2 elements to show the symmetry correspondence. The bond designations are only approximate (e.g., $[2a_g^2]_{\sigma_{NN}}$ and $[3a_g^2]_{\sigma_{NH}}$ are probably mixed).[5] The measured results of this work are summarized below. A discussion of the correlations of excited states and geometries on reactivity is presented in greater depth in Sec. IV.

$N_2H_3^+$ *fragment.* The H atom dissociation in NH_3 ionization has been attributed to internal conversion from the first excited ion electronic state $\tilde{A}$.[11,22] The H atom threshold for $N_2H_4^+$ occurs well below analogous excited states due to σ_{NH} electron ionization. Direct ground state dissociation is possible in $N_2H_4^+$ because of the unusually broad Franck–Condon ionization band which can produce ions with internal energy exceeding the $N_2H_3^+$–H bond energy of 2.8 eV (Refs. 24, 57) [note that the vIP exceeds the aIP by nearly 2 eV, Eq. (16)]. A similar mechanism does not exist for NH_3 because of the large NH_2^+–H bond energy of 4.9 eV (Ref. 10) and the narrower Franck–Condon band for ionization (vIP−aIP=0.7 eV).

$N_2H_2^+$, N_2H^+, N_2^+, H_2^+, H^+ *fragments.* The observed thresholds for $N_2H_2^+$ and N_2H^+ are consistent with sequential H atom loss (Table III). However, a concerted dissociation to form $N_2H_2^+ + H_2$ (two-body) and $N_2H^+ + H_2 + H$ (three-body) is possible if the observed thresholds actually correspond to $^2B_{1g}(3a^{-1})$ and $^2B_{2u}(3b^{-1})$ electronic state excitation, which are believed to correlate with H_2 production (Sec. IV A). A comparison of observed and calculated thermochemical thresholds for N_2^+ implies a double-elimination reaction to give $N_2^+ + 2H_2$. A similar threshold value was observed by Dibeler *et al.*.[28] This result, however, seems to conflict with the high threshold of 50 eV observed for H_2^+, if one assumes that some charge transfer should take place to produce H_2^+ from N_2^+. (H_2 and N_2 have IPs of 15.4 and 15.6 eV, respectively).[58] The possibility of an N_2 impurity is unlikely because of the strength of the N_2^+ signal, the absence of a dissociative fragment N^+, and because N_2^+ is formed with substantial KE (Fig. 14). A reaction mechanism that leads to N_2^+ without invoking H_2^+ and that explains the similarity of the H^+ and N_2^+ thresholds is discussed in Sec. IV B.

NH_3^+ and NH_2^+ fragments. The presence of NH_3^+ is

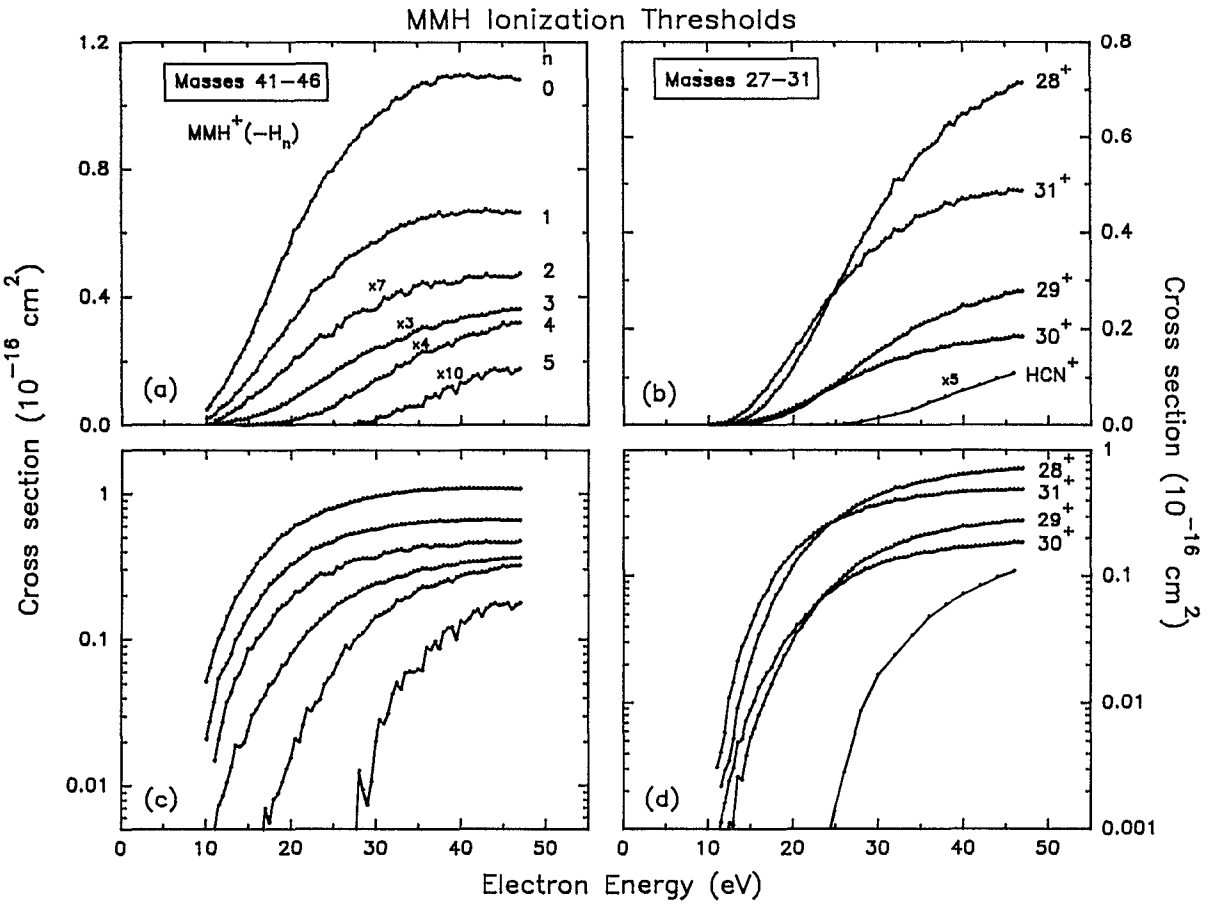

FIG. 16. Dissociative-ionization cross sections for the larger fragments of MMH recorded at higher resolution in the threshold region. (a),(b) and (c),(d) are linear and log σ scales, respectively.

believed to result from a 1,2 hydride shift followed by N–N bond scission (Sec. IV B). NH_2^+ may possibly form by simple bond scission of an unrearranged $N_2H_4^+$. It is interesting to note that NH_4^+ has a very low thermochemical threshold (Table III), but N_2H_4 is geometrically constrained from forming this product. This restriction is relaxed for MMH.

3. Fragment kinetic-energy distributions

The KE distributions for N_2H_4 dissociative ion fragments are plotted in Fig. 14 and $\langle \epsilon_t \rangle$ values summarized in Fig. 6(b). The results differ from those measured for NH_3 ionization in the following ways: (1) The set of $\langle \epsilon_t \rangle$ values are significantly less for N_2H_4; (2) there is less variation in the $\langle \epsilon_t \rangle$ for different fragments for N_2H_4 ionization; (3) except for H^+, all fragment velocity probabilities $P(v)$ are very much Gaussian in dependence. These observations are consistent with a statistical dissociation, whereby the excess excitation energy above the thermochemical threshold is distributed over all the internal and translational degrees of freedom (Sec. IV B).

The increasing KE for the lighter fragments is a kinematic effect of conservation of momentum.[49] In fact, the c.m. KE, assuming a two-body dissociation are comparable for nearly all dissociations, including H^+, which does not exhibit a Gaussian-type velocity probability. The major exception to this trend is H_2^+, which has an anomalously low KE. This fragment also has an unusually high threshold potential as mentioned before (Fig. 12, Table II). Reaction mechanisms are discussed in Sec. IV B.

C. MMH results

1. Dissociative-ionization cross sections

The total EI ionization cross sections for MMH are given in Fig. 7. The magnitude is similar to N_2H_4 (σ_{tot} = 4.20 Å^2 vs 3.76 Å^2), but the shape is slightly different and the low-energy band is more pronounced and centered at lower energy (35 eV vs 41 eV). Partial cross sections for ion fragments are given in Figs. 15–17. The analysis of the MMH fragment ions is complicated by the existence of different fragments of the same mass [because $m(N) = m(CH_2)$] and by the two sources of H atom loss [N–H and C–H].

$MMH(-H_n)^+$ n=0–5 ion signals. The designation for these ions denotes loss of n number of H atoms. The parent ion signal MMH^+ shows a band at 40 eV that is more pronounced than that observed for N_2H_4 or NH_3. This feature also appears in the cross section curves for fragments n=1 and 2. All fragment curves have peak cross

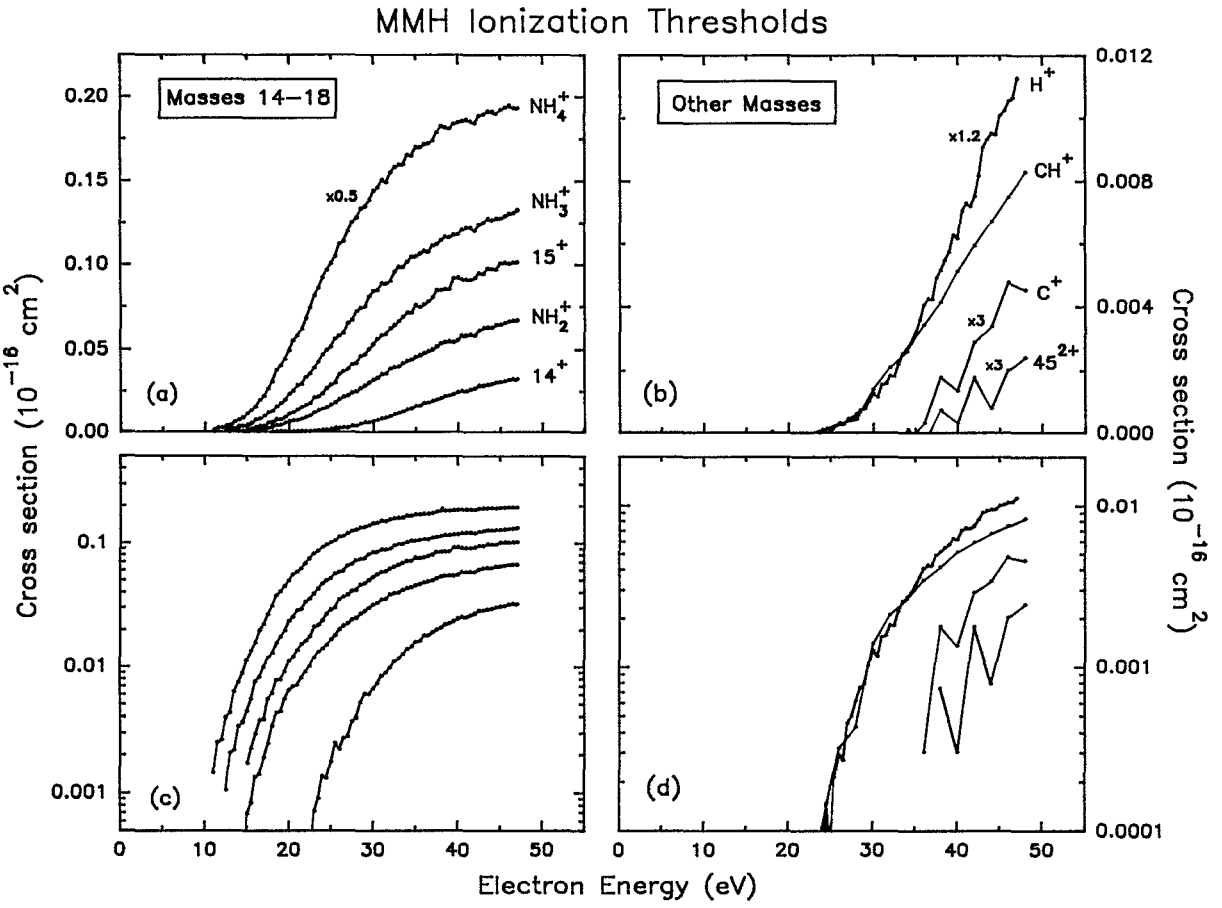

FIG. 17. Dissociative-ionization cross sections for the smaller fragments of MMH recorded at higher resolution in the threshold region. (a),(c) and (b),(d) are linear and log σ scales, respectively.

sections that shift to higher electron energy as n increases (with the exception of $n=2$). There is also a monotonic decrease in cross section with increasing n except for the anomalously low value for $n=2$.

Ion fragment masses 27–31. This series of ions have contributions from CNH_{6-n}^+ (masses 26–32) and $N_2H_{6-n}^+$ (masses 28–34). Calculated thermochemical thresholds are compiled in Table IV. These sequences of fragment ions, which are separated by 0.013 amu, were resolved using a high resolution quadrupole mass spectrometer.[59] The relative intensities are reported in Table V. As mentioned in Sec. II, the measured relative intensities are not quantitative due to strong KE discrimination effects that occur at high instrumental mass resolution. Still, the measurements are important for observing trends. At 15 eV, the CNH_{6-n}^+ series dominates over the $N_2H_{6-n}^+$ series for masses 28–30, but $N_2H_3^+$ dominates over $CH_2NH_3^+$ for mass 31. These results are consistent with the calculated thermochemical thresholds reported in Table IV. As electron energy increases, the $N_2H_{6-n}^+$ series increases in intensity much faster than the CNH_{6-n}^+ series, such that the former series dominates at $E \geqslant 70$ eV for masses 29–31. Interestingly, for mass 28, only a negligible amount of N_2^+ is observed at any energy, in contrast to the case of N_2H_4 ionization. Instead, the stable structure $CH{\equiv}NH^+$ accounts for the mass 28 signal. Simple CH_3 dissociation to give $N_2H_3^+$ accounts for most of ion fragment mass 31 and is consistent with the absence of a signal at mass 32. The other mass 31 fragment $CH_2NH_3^+$ is formed by a 1,2 hydride shift and N–N dissociation, in analogy to NH_3^+ formation in N_2H_4 ionization. A stable $CH_2{=}NH_2^+$ ion can then form by hydrogen dissociation, which may explain the low yield of $CH_2NH_3^+$. The importance of rearrangement mechanisms for MMH^+ dissociation is considered in greater depth in Sec. IV B.

Ion fragment masses 12–18. These ions are accounted for by the structures NH_m^+ and CH_m^+. Masses 17 and 18 are explained by fragments NH_3^+ and NH_4^+. Mass 16 is due primarily to NH_2^+, even though CH_4^+ has a much lower thermochemical threshold (Table IV). A distinct crossover develops in which the ion signals for masses 12–15 arise almost entirely from fragments CH_m^+ $m=0$–3. The increase in intensity for mass 15 relative to 16 (Fig. 15) is consistent with the presence of two monotonically decreasing series of ion signals corresponding to NH_m^+ ($m=2$–4) and CH_m^+ ($m=0$–3). Except for mass 16, these results conform to predictions based on thermochemical thresholds (Table IV).

H^+, H_2^+, and doubly charged ions. The relative cross section for H^+ production is comparable for MMH, N_2H_4,

TABLE IV. Thermochemical thresholds and appearance potentials for dissociative ionization of MMH.

Ion mass	Products	ΔH(eV)[a]	Electron impact	
			This work	Ref. 28[b]
45	$CH_3N_2H_2^+ + H$	10.59	10	10.2(9.8)
44	$CH_3N_2H^+ + H_2$	10.01	10.5	10.4(9.8)
	$+2H$	14.52		
43	$CH_3N_2^+ + H + H_2$	11.34	11.5	11.9,14.8(11.4)
	$+3H$	15.85		
42	$CH_2N_2^+ + 2H_2$	11.41	16.5	15.2
	$+H_2+2H$	15.92		
41	$CHN_2^+ + 2H_2 + H$	18.46		
	$+H_2+3H$	22.97	28	
	$+5H$	27.48		
31	$N_2H_3^+ + CH_3$	10.54	11	10.7(10.4)
	$CH_2NH_3^+ + NH$	<11.64		
	$CH_3NH_2^+ + NH$	11.64		
30	$CH_2NH_2^+ + NH_2$	8.70	11.5	11.2
	$CH_3NH^+ + NH_2$	9.61		
	$N_2H_2^+ + CH_4$	10.18		
29	$CHNH_2^+ + NH_3$	9.73	12.5	13.3
	$CH_2NH^+ + NH_3$	9.82		
	$N_2H^+ + CH_4 + H$	11.24		
28	$CHNH^+ + NH_3 + H$	10.61	12	13.2
	$CNH_2^+ + NH_3 + H$	12.30		
	$N_2^+ + CH_4 + H_2$	13.83		
27	$HNC^+ + NH_3 + H_2$	13.12	24	
	$HCN^+ + NH_3 + H_2$	13.55		
	$+NH_3+2H$	18.06		
18	$NH_4^+ + CHNH$	10.08	10.5	
17	$NH_3^+ + CH_2NH$	10.09	12	
	$CH_5^+ + N_2 + H$	10.65		
16	$CH_4^+ + N_2 + H_2$	10.78		
	$+N_2H_2$	12.84		
	$NH_2^+ + CH_2NH_2$	13.77	14.5	
15	$CH_3^+ + N_2 + H_2 + H$	12.62	14	
	$CH_3^+ + N_2H_3$	12.75		
	$NH^+ + CH_3NH_2$	16.18		
14	$CH_2^+ + N_2 + 2H_2$	13.38		
	$CH_2^+ + N_2H_4$	14.51		
	$+N_2H_3+H$	18.01	22	
	$N^+ + CH_3NH_2 + H$	20.48		
13	$CH^+ + N_2H_4 + H$	19.09		
	$+N_2H_3+2H$	22.59	24	
12	$C^+ + N_2H_4 + H_2$	18.70		
	$+N_2H_4+2H$	23.21		
	$+N_2H_3+3H$	26.71	33	
2	$H_2^+ + CH_2N_2H_2$	16.40		
	$+CH_2+N_2+H_2$	18.48		
1	$H^+ + CH_3 + N_2 + H_2$	16.39		
	$+CH_3+N_2+2H$	20.90	25	
45^{2+}	$CH_3N_2H_2^{2+} + H$	?	36	

[a]Values determined from heats of formation in Refs. 24, 25, and 58, and/or from thermodynamic cycles using data from Table III and Refs. 24, 25, 60, and 62.
[b]Values in parentheses are PI measurements from Ref. 26.

and NH_3 ionization. In contrast, the H_2^+ yield is extremely low ($\sigma < 10^{-19}$ cm^2) relative to the other ion fragment cross sections measured here. This result follows a trend toward increasing H_2^+ threshold potential for the series of molecules NH_3, N_2H_4, and MMH. Doubly charged fragment ions are observed in Fig. 18, the most abundant of which is $MMH(-H)^{2+}$. There is no evidence of the parent dication MMH^{2+}, even though this species is isoelectronic with methyl ethylene. It is also unclear why the dissociation of a neutral H atom from MMH^{2+} is relatively stable. Other signals at 22.0 and 21.5 mass-to-charge ratio are observed in an intensity ratio similar to that observed for the singly charged masses 45, 44, and 43.

2. Thermochemical and excited state thresholds

We make no attempt to derive an electron configuration for MMH as we did for N_2H_4 in Eq. (16), although similarities are expected. The nonbonding $n_\pm$ orbitals are still the highest occupied molecular orbitals and ionization

TABLE V. Comparison of relative intensities for common ions masses in the dissociative ionization of N_2H_4 and MMH for 100 eV excitation.[a]

	N_2H_4		MMH	
Ion mass	$\sigma(m^+)/\sigma(M^+)$	m	$\sigma(m^+)/\sigma(M^+)$[b]	m
31	0.37	$N_2H_3^+$	0.45, 0.05	$N_2H_3^+$, $CH_2NH_3^+$
30	0.34	$N_2H_2^+$	0.12, 0.10	$N_2H_2^+$, $CH_2NH_2^+$
29	0.33	N_2H^+	0.20, 0.10	N_2H^+, $CHNH_2^+$
28	0.12	N_2^+	0, 0.70	N_2^+, $CHNH^+$
18	<0.03	NH_4^+	0.19, 0	NH_4^+, CH_6^+
17	0.30	NH_3^+	0.15, 0	NH_3^+, CH_5^+
16	0.21	NH_2^+	0.075, 0	NH_2^+, CH_4^+
15	<0.02	NH^+	0.01, 0.10	NH^+, CH_3^+
14	<0.01	N^+	0, 0.047	N^+, CH_2^+
2	0.009	H_2^+	<0.001	H_2^+
1	0.065	H^+	0.024	H^+

[a]Data are not corrected for the KE detection efficiencies reported in Fig. 6.

[b]Fragments of the same nominal mass were resolved using a high resolution quadrupole mass spectrometer. The relative intensities are subject to uncertainties in the detection efficiency. The total signal strength at a single nominal mass was measured by TOF mass spectrometry and are reliable. Values of zero indicate intensities that are less than 5% of the main fragment signal.

of a lone-pair electron should cause a C_2 *gauche* to D_{2h} planar geometry change.[5] New and composite orbitals involving C-atom-centered atomic orbitals will exist for MMH. The higher-lying σ_{NH} orbitals are expected to lie just above the σ_{CH} orbitals on the basis of the lower IP for the N_2H_3 group (7.61 eV)[24] relative to the CH_3 group (9.84).[58] However, beyond this conjecture it is difficult to predict the threshold and other properties of the higher electronic states of MMH^+. Fortunately, the majority of measured fragment ion threshold potentials occur at sufficiently low energy to be attributed to hydrazinelike ion electronic states. The ion fragment threshold potentials for MMH ionization measured in Figs. 16 and 17 are compared to calculated thermochemical thresholds and to measured EI and PI values by Dibeler *et al.*[28] and Akopyan *et al.*,[26] respectively, in Table IV. The past and present experimental results are generally in good agreement, although threshold potentials for many more fragment ions are reported here.

$MMH(-H_n)^+$ $n=1$–5 ion signals. The low thresholds for $n>2$ are interesting because they seem to require a mechanism involving H_2 formation. Yet virtually no evidence of H_2^+ was observed. A similar difficulty was discussed for $N_2H_4^+$ dissociation to N_2^+ (Sec. III B 2 and Table III). The difficulty is relaxed somewhat for MMH^+ because the IPs of $MMH(-H_n)^+$ are much lower than N_2^+ and therefore not expected to favor charge transfer to H_2^+. It is also easier to envision H_2 formation in MMH^+ dissociation due to the greater number of H atoms in close proximity. Still the apparent facility of H_2 production may indicate extensive rearrangement before dissociation (Sec. IV B). Another possibility is that the $MMH(-H_n)^+$ fragments undergo a structural relaxation that lowers the actual calculated thermochemical thresholds. However, this would require a stabilization of about 4.5 eV, equal to the H_2 bond energy, to explain a lack of H_2 formation.

Ion fragment masses 28–31. These ions, and particularly the CNH_{6-n}^+ series, have very low computed thermochemical thresholds, but may experience an activation barrier as indicated by the observed thresholds. This is consistent with the need to break a strong N–N bond in the ion (about 5.6 eV). Interestingly, N_2H^+ is formed in large yield, even though it is significantly more endothermic than formation of $CHNH_2^+$. The appearance of N_2H^+ and $N_2H_2^+$ are explainable by a rearrangement and CH_4 elimination mechanism similar to that which leads to H_2 elimination above (also Sec. IV B). Finally, the threshold for mass 28 measured here and by Dibeler *et al.*,[28] which is anomalously low assuming N_2^+ production, is very reasonable for the fragment $CHNH^+$, which was discussed earlier to be the dominant mass-28 ion fragment for MMH ionization (Table V). We treat the N_2^+ vs $CHNH^+$ problem in greater depth in Sec. IV B.

NH_4^+ and NH_3^+. The presence of NH_4^+ implies a rearrangement involving extensive H atom migration facilitated by the methyl group. NH_4^+ is not observed, for example, in N_2H_4 ionization. The thermochemical threshold for producing NH_4^+ occurs at a rather low value of 10.1 eV for MMH (10.3 eV for N_2H_4) due to the large proton affinity of NH_3 (8.8 eV).[60,61] NH_3^+ is an energetically favorable product requiring less rearrangement than does NH_4^+ and is therefore observed in ample abundance for both N_2H_4 and MMH ionization (Sec. IV B).

H^+, H_2^+, and masses 12–16. The observed threshold potentials for ion masses 15 and 16 are near to the lowest energy thermochemical thresholds, however, a large jump upward in energy occurs for the lighter masses. These high thresholds are consistent with either excited electronic-state effects or more likely multiple dissociation. The threshold for C^+ is very similar to that of the doubly charged fragment $MMH(-H)^{2+}$ and may in part be formed by Coulomb repulsion in the MMH^{2+} dication. The absence of H_2^+ and the high 25 eV threshold potential of H^+ is to be contrasted with the moderate presence of H_2^+ and the lower 18 eV threshold potential of H^+ for

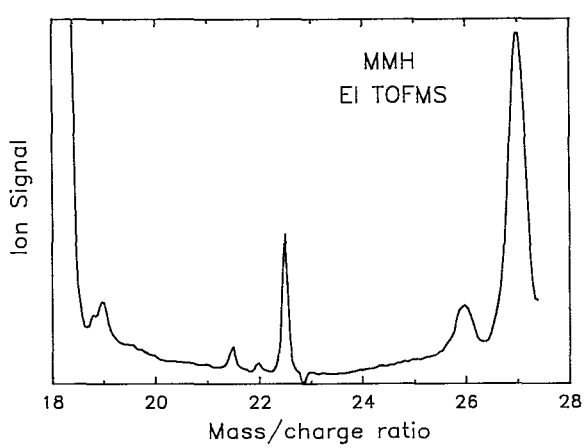

FIG. 18. TOF mass spectrum of MMH in the vicinity of the doubly charged ion signals. Also note KE broadening of the TOF peak shape for masses 26 and 27.

N_2H_4 ionization. This result is consistent with a charge transfer mechanism whereby the charge is more likely to reside on the larger fragment since it usually has the lower IP (particularly if it has nonbonding orbitals).

3. Fragment kinetic energy

The kinetic-energy distributions for MMH ion fragmentation are too numerous to show. Instead we summarize the $\langle \epsilon_t \rangle$ values in Fig. 6(c) along with results for N_2H_4 and NH_3 ionization. The less energetic fragments are well described by Gaussian velocity probabilities. This dependence becomes noticeably distorted for ion masses 1, 12, 13, 14, and 27. A few general trends are noted in the following:

(1) The $\langle \epsilon_t \rangle_{\text{c.m.}}$ values for MMH^+ fragment ions that also occur by N_2H_4 ionization are smaller, which is consistent with a statistical interpretation of energy redistribution that excess energy is partitioned equally among all degrees of freedom. Therefore, the fraction of energy appearing as KE should decrease as the molecular size increases. However, the decrease in magnitude (which was large for N_2H_4 relative to NH_3) is much less for MMH relative to N_2H_4.

(2) There is a trend toward greater kinetic energy for the less abundant fragment ions. These ions typically have higher thermochemical threshold potentials. Even for excitation energies above threshold, the yield of the high-energy fragments is expected to be small relative to low-energy fragments due to entropy and density of state arguments and only becomes large well above threshold (in analogy to Boltzmann-equilibrium populations of high-energy states). Consequently, high-energy fragments are typically formed with considerable energy, so the statistical fraction appearing as kinetic energy can, therefore, be substantial.

(3) Kinetic-energy measurements are important for establishing the origin of fragment ions that could also arise from impurity ionization. It should be recalled that H_2 impurity plagued several previous studies of NH_3 ionization (Sec. III A 1). The fragment ions NH_3^+ and NH_4^+ are difficult to explain by simple reaction mechanisms, as discussed earlier. However, significant KEs were measured for these ions, which argues against the likelihood that they are parent ions or originate from impurities.

(4) Although the dependence of fragment KE on electron energy was not studied systematically, a small sampling of results were collected to test the reasonableness of the KE measurements and to check for any unusual affects in the measurement technique. Values of $\langle \epsilon_t \rangle$ were measured for ion masses 18, 16, and 15 for MMH ionization at electron energies of 35, 70, and 170 eV. The following $\langle \epsilon_t \rangle$ values were obtained as a function of increasing electron energy: 0.045, 0.066, and 0.075 (mass 18); 0.073, 0.15, 0.18 eV (mass 16); and 0.12, 0.18, and 0.18 eV (mass 15). These results are consistent with the qualitative expectation that increasing electron energy will populate a larger fraction of the higher-excited electronic states, but that the electronic-state distribution should level off when the electron energy greatly exceeds the highest energy accessible state [$\simeq$30 eV for hydrazines, cf. Eq. (16)]. This leveling off occurs at about 70 eV electron energy.

IV. DISCUSSION

A. Electronic structure, geometry, and correlations to dissociation

In Paper I, geometry was described as having a major role in explaining electronic and reactive properties of hydrazine.[5] The geometry of the neutral ground electronic state has pyramidal nitrogen bonds (like NH_3) and a dihedral N–N bond angle θ of about 95° between the nonbonding orbitals (an approximately *gauche* conformation).[29,50,55] The range of calculated rotational barriers at 0° (C_{2v}, syn conformer) and 180° (C_{2h}, anticonformer) is 0.42–0.59 and 0.07–0.27 eV, respectively.[51,52,55] The planar D_{2h} energy is not known, but is expected to be at much higher energy than the other conformers because the $n_\pm$ orbitals would correspond to fully occupied π and π^* orbitals. Ionization of a $n_\pm$ electron removes a potential π^* repulsion, which stabilizes the D_{2h} planar geometry for the $N_2H_4^+$ ground state. The difference in energy between the planar D_{2h} and the pyramidal *gauche* C_2 geometry in the ground state ion is 1.7 eV determined from the difference in the measured vIP and aIP.[26,56]

The electronic configuration for N_2H_4 is given in Eq. (16). The calculated dependence of the $N_2H_4^+$ ion electronic states on the N–N dihedral angle θ is given in Fig. 19. These curves were derived by subtracting the orbital energy of the ionized electron from the ground state potential (Koopman's assumption)[61] using *ab initio* data by Fink *et al.*[55] We show the D_{2h} electronic state designations that correlate to the C_{2v} ($\theta=0°$), C_2 ($0<\theta<180°$), and C_{2h} ($\theta=180°$) states. Figure 19 describes a neutral ground state ^1A that has a moderately shallow mimina at $\theta=90°-100°$, and an ionic ground state that is very unstable at this angle. Unfortunately, no calculations exist for the planar D_{2h} geometry. However, it is well established that the ground state ion is of D_{2h} geometry and that the π–π^* splitting corresponding to the $^2B_{1u}$–$^2B_{2g}$ energy gap is over 6 eV.[53,54]

We have drawn simple representations of the MOs for the unpaired electron for each of the electronic states in Fig. 19. These pictures are instructive for understanding the geometric energies for each state and more importantly for deducing relative bond strengths and correlations to dissociative fragments. It is interesting to note that some of the excited electronic states interconvert by N–N bond rotation. This property is a potentially important mechanism for producing sufficient internal energy to break bonds. Using the energy diagram and MO pictures in Fig. 19, we provide an interpretation of the role that each state plays in dissociation. We then discuss some weaknesses and unresolved issues resulting from this simple analysis.

$^2B_{2g}$–$^2B_{1u}$. These states derive from $n_\pm$ electron ionization [Eq. (16)] and are separated in energy by about 6–7 eV based on measured π,π^* transition frequencies in solution and on measured ESR hyperfine splittings of the unpaired electron.[53,54] Excitation of the upper $^2B_{1u}$ state

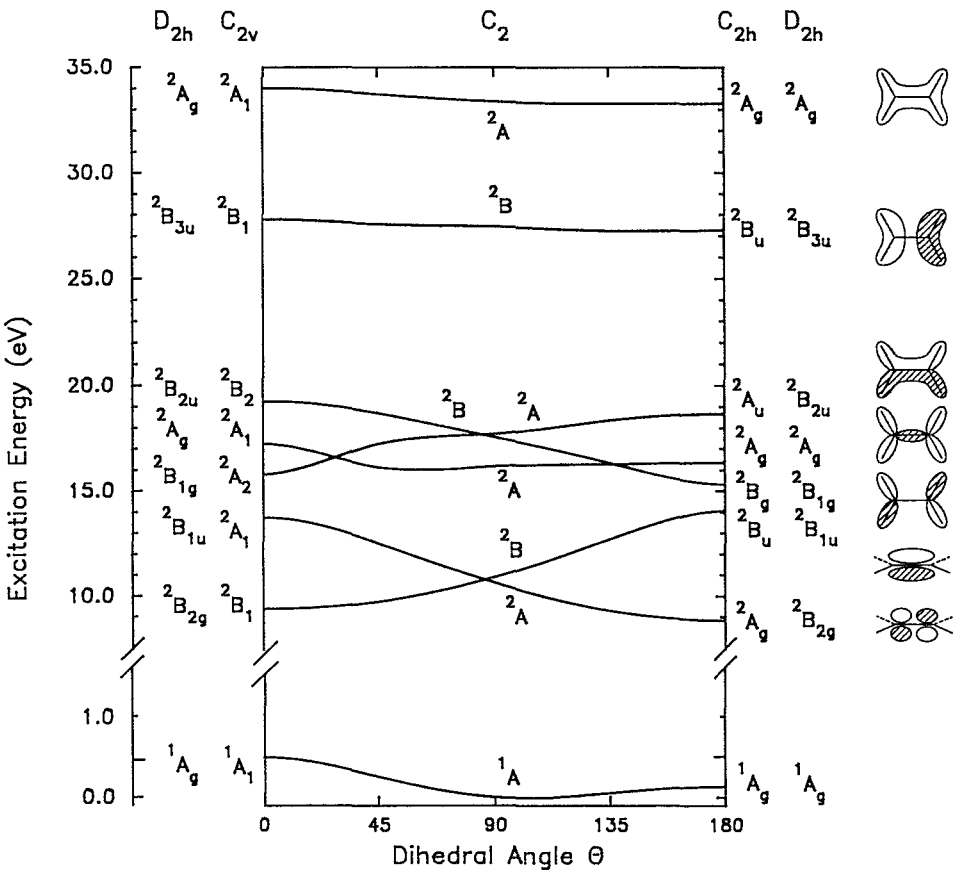

FIG. 19. $N_2H_4^+$ electronic state energy dependence on the N–N rotation angle θ. The curves were computed from the orbital energy calculations of Fink *et al.* (Ref. 55). A spline fit was made to the calculated values of $\theta=0°$, 45°(−45), 90°, 135°(−135), 180°. The D_{2h} symmetries for planar N_2H_4 are shown alongside the corresponding C_{2v} and C_{2h} elements. Energies are relative to neutral ground electronic state ^1A. The axis system is defined such that z is the out-of-plane C_2 symmetry rotation axis and x and y are the long (N–N) and short axis in the molecular plane.

should lead to free rotation to the $^2B_{2g}$ state with large excess energy that can relax into rovibrational states and cause dissociation. It is not clear whether the $^2B_{1u}$, though formally allowed, is directly excited by EI excitation. Ionization of the b_{1u}, n_- electron [Eq. (16)] correlates with both the $^2B_{1u}$ state (rotation to $\theta=180°$) and the $^2B_{2g}$ ground state (rotation to $\theta=0°$). Hence, ionization of either the n_+ or n_- electron is likely to produce the $^2B_{2g}$ ground state. The upper $^2B_{1u}$ state may be populated by internal conversion from a higher excited state. According to the MO picture in Fig. 19, the removal of a π^* electron to form the ion ground state $^2B_{2g}$ is expected to substantially increase the N–N bond strength and have a less certain affect on the N–H bond energy. Indeed, the reported N–N bond energy increases from 2.84 in the neutral to 5.62 eV in the ion, and the N–H bond energy decreases from 3.50 to 2.75 eV.[24,25,57] The ground state $^2B_{2g}$ should correlate with H atom dissociation and because of the unusually broad Franck–Condon band for ionization of N_2H_4 to $^2B_{2g}$, direct excitation above the N–H dissociative limit is possible, unlike the case for NH_3 ionization noted earlier (Sec. III B 2). The removal of a π electron to form the $^2B_{1u}$ ion state will considerably weaken the N–N bond strength relative to the ground state energy of 2.84 eV and may in fact be dissociative along this coordinate. The $^2B_{1u}$ state should have a strong correlation to formation of NH_2^+ if it does not undergo rapid internal rotation to $^2B_{2g}$ (Fig. 19).

$^2B_{1g}$–$^2B_{2u}$. These states derive from σ_{NH} orbitals that have a major component from $2p_yN$ (symmetric and antisymmetric combinations of the two nitrogen orbitals), thus explaining the fairly large energy dependence on θ. Interconversion from $^2B_{2u}$ to $^2B_{1g}$ by rotation can deposit >3 eV of energy into internal excitation based on the calculated energies in Fig. 19. The N–H bond is clearly weakened in both states due to the removal of a bonding σ_{NH} electron; however, the node between geminal 1,1 hydrogens argues for an increased H–H bonding interaction (i.e., a decreased antibonding interaction). This could promote H_2 formation by either 1,1 (geminal) or 1,2 hydrogen elimination (the latter possibility for $^2B_{1g}$ only). The surprisingly low appearance potential for N_2^+ (Table III) implies formation of H_2. The $^2B_{1g}$ and $^2B_{2u}$ states are plausible avenues for such a dissociation.

^2A_g. This state is formed by removing an electron from a σ_{NH} orbital that has a major $2p_xN$ component (symmetric combination), thus explaining the relative insensitivity of energy to θ (Fig. 19). The ^2A_g state cannot convert to

the antisymmetric combination state $^2B_{3u}$ by any rational geometry change. But it does mix somewhat with the higher-lying ^2A_g state nominally associated with a σ_{NN} orbital. The molecular orbital picture in Fig. 19 predicts for ionization to ^2A_g a significant weakening of the N–H bond, a lesser weakening of the N–N bond, and a greater repulsion between the H atoms. There is no clear correlation to a single product; multiple H atom dissociation seems possible. Of the four σ_{NH} states, the ^2A_g state in this model is the most likely one to lead to N–N bond dissociation products.

$^2B_{3u}$. This state is the highest-lying σ_{NH} state and corresponds to removal of an electron from an orbital with a major $2sN$ component, explaining the insensitivity to θ (Fig. 19). The MO model predicts a weaker N–H bond, a stronger N–N bond, a repulsion of the geminal hydrogens, and an attraction between the *cis* 1,2 hydrogens. A correlation to multiple H atom dissociation or 1,2 elimination seems plausible.

^2A_g. This higher-lying ^2A_g state corresponds to removal of an electron from a nominally σ_{NN} orbital with some σ_{NH} mixing from the lower-lying ^2A_g state as discussed above. Ionization to this state weakens the N–N bond significantly, weakens the N–H bond to a lesser extent, and increases repulsion between the H atoms. These properties suggest a product correlation involving N–N bond breaking or multiple H atom dissociation.

The above arguments are based on simple molecular orbital concepts that overlook other potentially important dynamics, a few of which we mention. (1) Ionic structures can rearrange before dissociating and apparently do so according to the evidence collected in this work. The molecular orbital picture is very useful for explaining these mechanisms as discussed below. (2) Excitation at energies within 10–20 eV of the ionization threshold can populate neutral excited states in competition with ionization that either dissociate to neutral fragments or undergo autoionization. These states include Rydberg excitations that converge to the σ_{NH} and σ_{NN} ionization thresholds (Fig. 19). Rydberg autoionization/dissociation was invoked by Locht *et al.* for electron excitation of NH_3 (Sec. III A 2).[22]

B. Rearrangements and reaction mechanisms

Rules for understanding rearrangement reactions in terms of MO theory are frequently treated in physical-organic text books.[63,64] Migration is most likely to occur through interactions with vacant or partially filled orbitals, which explains the propensity of rearrangement reactions in ions, radicals, and photoexcited molecules. A common treatment is to examine, using symmetry concepts, whether the unfilled orbital of the migrating group undergoes a bonding or antibonding interaction with the molecular backbone for some reasonable transition state structure. A mechanism often exists for migration of a σ orbital (i.e., alkyl or H atom group) across a π bond; the issues are mainly a question of whether the group stays on one side of the molecular plane (i.e., as for a π orbital, suprafacial) or is forced to break the plane to maintain bonding (i.e., for a π^* orbital, antarafacial). These issues determine stereochemistry, which is not a concern of this discussion. There is usually some pathway for rearrangement in ions that is symmetry allowed; hence, discussion here is reduced to considering whether the rearranged structures are energetically feasible.

1,2 sigmatropic shift. The $N_2H_4^+$ ion is planar and has a singly occupied π^* orbital that can serve as a conduit for migration of a H atom (singly occupied σ orbital). We consider the following rearrangement:

$$H_2N\overset{1.450}{-}NH_2 \underset{8.1\ eV}{\rightarrow} [H_2N\overset{1.291}{-}NH_2]^+ \underset{1.2\ eV}{\rightarrow} HN\overset{1.437}{-}NH_3^+,$$

where the IP (Ref. 56) and calculated bond lengths and rearrangement energy are indicated.[65] The thermodynamic threshold of 12.45 eV calculated for NH_3^+ formation (Table III) indicates a HN–NH_3^+ bond energy of 3.15 eV. This is a reasonable value if we consider that H_2N–NH_2 has a similar bond length and a bond energy of 2.8 eV.[24] The N–H bond energies in HN–NH_3^+ are expected to be >3.5 eV based on reported bond energies for NH_2 and NH_4^+.[60,61] Thus N–N is the most likely bond to break and the 1,2 hydride shift is therefore the most probable mechanism leading to NH_3^+ product. A similar reaction can be envisioned for MMH ionization by the sequence

$$H_2N\text{–}NHCH_3 \underset{7.7\ eV}{\rightarrow} [H_2N\text{–}NHCH_3]^+ \rightarrow HN\text{–}NH_2CH_3^+.$$

The 1,2 hydride shift in MMH^+ is aided by the lowering of the nitrogen-orbital IP due to methylation, hence, the rearrangement energy should be less than is the case for $N_2H_4^+$. In addition to N–N bond dissociation, there is evidence to suggest that other rearrangement and dissociation reactions occur for MMH^+. From a purely thermochemical standpoint, formation of NH_4^+ is calculated to be the lowest energy fragmentation channel for N_2H_4 and one of the lowest for MMH ionization (Tables III and IV). The enormously different yields of NH_4^+ for these two molecules (Table V) indicates that the methyl group facilitates and acts as a source of additional rearrangement channels in MMH^+.

Elimination reactions. Evidence suggests that extensive elimination occurs for MMH^+, but not for $N_2H_4^+$ (other than for the special case of N_2^+ formation discussed below). For H atom loss, the threshold potentials are consistent with a sequential mechanism for N_2H_4 ionization and a concerted mechanism, forming H_2, for MMH ionization. (The alternative explanation for N_2H_4 is that the observed thresholds correspond to high electronic state excitation, which can undergo concerted elimination). Eliminations are favored in cases where a stable double bond can form. For MMH, a 1,2 H_2 elimination across the N–C bond is expected, which forms a stable $H_2C{=}NNH_2^+$ ion. Elimination is less favored across the N–N bond of the parent ion because of the partial double bond character that already exists $\{[\pi]^2[\pi^*]^1$ configuration, Eq. (16)$\}$. KE measurements are also consistent with a H_2 elimination mechanism for H atom loss. In Fig. 6(c), the $\langle\epsilon_t\rangle$ value for $H_2C{=}NNH_2^+$ corresponds to a $\langle\epsilon_t\rangle_{c.m.}$ value of about 0.6

eV, if we assume a two-body dissociation. Assuming a multibody (sequential) dissociation implies a much larger $\langle \epsilon_t \rangle_{c.m.}$ value, which seems excessive compared to the $\langle \epsilon_t \rangle_{c.m.}$ values of other fragments. An elimination reaction leading to CH_4 is also evident for MMH^+ based on comparison of observed and calculated thermochemical thresholds for the fragment ions $N_2H_2^+$ and N_2H^+. A plausible mechanism is 1,2 elimination by the route

$$H\text{–}HNNH\text{–}CH_3^+ \rightarrow HN{=}NH^+ + CH_4 .$$

A 1,1 elimination is possible, but judged less likely because the resultant ion structure $H_2N{=}N^+$ is about 0.2 eV less stable[57] than $HN{=}NH^+$ and because 1,2 eliminations are far more common throughout chemistry.[64] However, a 1,1 elimination from the hydride-shift ion structure $HN\text{–}NH_2CH_3^+$, discussed above, could give the favored $HN{=}NH^+$ ion structure.

Concerted mechanism for N_2^+ formation. An apparent conflict between the observed and calculated thermochemical thresholds of mass 28 was described earlier (Secs. III B and III C, respectively) for N_2H_4 and MMH ionization. High resolution mass spectra of MMH recorded at 100 eV electron energy reveal that the mass-28 ion signal is composed of $CHNH^+$ with little evidence of N_2^+.[59] This result resolves the mystery of the low threshold potential measured here and by Dibeler *et al.*[28] (Table IV). For N_2H_4 ionization, the presence of ion mass 28 can only be explained by N_2^+, which must form by one, if not two, H_2 elimination reactions to explain the low chemical threshold (Table III). There are several reasons to believe the measured potentials are real. (1) Similar values were measured by Dibeler *et al.* (2) Their work used ambient samples, which rules out the possibility of a cluster reaction in our work. (3) N_2 impurity is unlikely because the measured threshold is higher than the IP of N_2. (4) Large kinetic energies were measured for N_2^+ suggesting that they are fragments. A rational reaction mechanism can be made that is consistent with other observed properties. We consider excitation of N_2H_4 to the interconverting $^2B_{1g}$–$^2B_{2u}$ states (Fig. 19), which correlate to concerted H_2 dissociation (Sec. IV A). The combination of excess excitation energy, made possible by the large Franck–Condon region, and relaxation energy by rearrangement is sufficient to dissociate H_2. The $HNNH^+$ fragment carries the charge in this first step [HNNH and H_2 have IPs of 9.6 (Ref. 24) and 15.5 eV, respectively], thus explaining the absence of H_2^+ at low excitation energies. The low threshold energy measured for N_2^+ is only compatible with another concerted H_2 elimination, however, it is likely that some sequential H atom dissociation occurs at higher energy, although we have no direct evidence for this. Sequential loss of H atoms (and alkyl groups) is supported by studies of gas-phase decomposition of azo compounds R–NN–R′.[66] It is uncertain why N_2^+ is not formed by MMH ionization. High resolution mass spectra of hydrazines and similar molecules are currently underway to help address these and other mechanistic issues.[59]

V. CONCLUSIONS

We have presented a comprehensive set of ionization data for hydrazine molecules and ammonia. The principal measurements are absolute partial cross sections for dissociation ionization as a function of electron energy. Measurements of threshold potentials and kinetic energies are also reported for all fragments studied. Together, these data form a valuable basis for deciphering ion fragmentation mechanisms and for testing simple molecular-orbital and electronic-state models for dissociation of these ions. Aside from serving as an exhaustive data base, some interesting reaction mechanisms were learned. The observation of NH_3^+ and the measured value of the threshold potential is evidence for a 1,2 hydride shift to form $HN\text{–}NH_3^+$, which then dissociates. Additional rearrangement mechanisms are apparent for MMH^+. A 1,2 H_2 elimination across the C–N bond is supported by the observed threshold measurements and the predicted stability for the fragment ion $H_2C{=}NNH_2^+$. Threshold measurements are also supportive of an elimination reaction yielding CH_4 as a product.

The use of crossed electron–molecular beam, pulsed ion extraction, and multichannel (TOF) mass detection has many advantages over conventional techniques and it is believed that the data presented here amply demonstrate the utility of this technique for measuring dissociative-ionization cross sections. The measurements of threshold potentials and kinetic energies were secondary objectives that did not employ the full capabilities of the apparatus. For example, only after the experiments were completed was it realized that the ion-deflection measurements could be used to determine fragment kinetic energies. There are several routine implementations in progress that will improve these measurements significantly in terms of energy resolution, uniformity of collection efficiency, and sensitivity. Likewise, a number of refinements are being developed to obtain similar improvements in the threshold measurements.

ACKNOWLEDGMENTS

I am grateful to Dr. Brian Brady for recording the high resolution mass spectra of MMH and to the referee for making several crucial comments regarding the MMH dissociative-ionization thermochemistry. This work was supported by the Aerospace Sponsored Research program.

[1] M. Schürgers and K. H. Welge, Z. Naturforsch. Teil A **23**, 1508 (1968); H. Biehl and F. Stuhl, J. Photochem. Photobiol. A **59**, 135 (1991).
[2] V. Staemmler, Acta Phys. Pol. A **74**, 331 (1988); E. M. Evleth and E. Kassab, J. Am. Chem. Soc. **100**, 7859 (1978).
[3] C. Willis and R. A. Back, Can. J. Chem. **51**, 3605 (1973); D. A. Ramsey, J. Phys. Chem. **57**, 415 (1953); G. S. Chandler and A. D. McLean, J. Chem. Phys. **71**, 2175 (1979).
[4] P. Lindberg, D. Raybone, J. A. Salthouse, T. M. Watkinson, and J. C. Whitehead, Mol. Phys. **62**, 1297 (1987); W. G. Hawkins and P. L. Houston, J. Phys. Chem. **86**, 704 (1982); M. Arvis, C. Devillers, M. Gillois, and M. Curtat, *ibid.* **78**, 1356 (1974).
[5] J. A. Syage, R. B. Cohen, and J. Steadman, J. Chem. Phys. **97**, 6072 (1992).
[6] K. H. Becker and K. D. Bayes, J. Phys. Chem. **71**, 371 (1967); F. E.

Logan and J. M. Marchello, J. Chem. Phys. **49**, 3929 (1968); M. Gehring, K. Hoyermann, H. Schacke, and J. Wolfrum, *14th Symposium (Int.) on Combustion* (The Combustion Institute, Pittsburgh, 1972), p. 99; S. N. Foner and R. L. Hudson, J. Chem. Phys. **49**, 3724 (1968); **53**, 4377 (1970).

[7] J. A. Syage, Phys. Rev. A **46** (1992); J. A. Syage, J. Phys. B **24**, L527 (1991).

[8] J. A. Syage, J. Chem. Phys. **92**, 1804 (1990); J. A. Syage and J. Steadman, Rev. Sci. Instrum. **61**, 1204 (1990); J. A. Syage, J. E. Pollard, and J. Steadman, Chem. Phys. Lett. **161**, 103 (1989).

[9] J. A. Syage Chem. Phys. Lett. **143**, 19 (1988).

[10] J. A. R. Samson, G. N. Haddad, and L. D. Kilcoyne, J. Chem. Phys. **87**, 6416 (1987).

[11] G. R. Wight, M. J. Van der Wiel, and C. E. Brion, J. Phys. B **10**, 1863 (1977).

[12] P. L. Kronebusch and J. Berkowitz, Int. J. Mass Spectrom. Ion Phys. **22**, 283 (1976); K. E. McCulloh, *ibid.* **21**, 333 (1976).

[13] J. W. Rabalais, L. Karlsson, L. O. Werme, T. Bergmark, and K. Siegbahn, J. Chem. Phys. **58**, 3370 (1973).

[14] M. J. Weiss and G. M. Lawrence, J. Chem. Phys. **53**, 214 (1970); G. R. Branton, D. C. Frost, F. G. Herring, C. A. McDowell, and I. A. Stenhouse, Chem. Phys. Lett. **3**, 581 (1969); A. W. Potts and W. C. Price, Proc. R. Soc. London, Ser. A. **326**, 181 (1972).

[15] T. J. Xia, T. S. Chien, C. Y. Robert Wu, and D. L. Judge, J. Quant. Spectrosc. Radiat. Transfer **45**, 77 (1991); V. H. Dibeler, J. A. Walker, and H. M. Rosenstock, J. Res. Natl. Bur. Stand. A **70**, 459 (1966); K. Watanabe and J. R. Mottl, J. Chem. Phys. **26**, 1773 (1957); K. Watanabe, *ibid.* **22**, 1564 (1954).

[16] K. Bederski, L. Wójcik, and B. Adamczyk, Int. J. Mass Spectrom. Ion Phys. **35**, 171 (1980).

[17] T. D. Märk, F. Egger, and M. Cheret, J. Chem. Phys. **67**, 3795 (1977).

[18] A. Crowe and J. W. McConkey, Int. J. Mass Spectrom. Ion Phys. **24**, 181 (1977).

[19] J. Gomet, C. R. Acad. Sci. Ser B **281**, 627 (1975).

[20] L. E. Melton, J. Chem. Phys. **45**, 4414 (1966).

[21] M. M. Mann, A. Hustrulid, and J. T. Tate, Phys. Rev. **58**, 340 (1940).

[22] R. Locht, Ch. Servais, M. Ligot, Fr. Derwa, and J. Momigny, Chem. Phys. **123**, 443 (1988); R. Locht, Ch. Servais, M. Ligot, M. Davister, and J. Momigny, *ibid.* **125**, 425 (1988); R. Locht and J. Momigny, *ibid.* **127**, 435 (1988).

[23] D. Morrison and J. C. Traeger, Int. J. Mass Spectrom. Ion Phys. **11**, 277 (1973).

[24] B. Ruscic and J. Berkowitz, J. Chem. Phys. **95**, 4378 (1991).

[25] S. T. Gibson, J. P. Greene, and J. Berkowitz, J. Chem. Phys. **83**, 4319 (1985).

[26] M. E. Akopyan and F. I. Vilesov, Engl. trans. Kinet. Catal. **4**, 32 (1962); M. E. Akopyan, F. I. Vilesov, and A. N. Terenin, Bull. Acad. Sci. USSR Phys. Ser. **27**, 1504 (1963).

[27] S. N. Foner and R. L. Hudson, J. Chem. Phys. **68**, 3162 (1978).

[28] V. H. Dibeler, J. L. Franklin, and R. M. Reese, J. Am. Chem. Soc. **81**, 68 (1959).

[29] K. Osafune, S. Katsumata, and K. Kimura, Chem. Phys. Lett. **19**, 369 (1973).

[30] N. Bodor, M. J. S. Dewar, W. B. Jennings, and S. D. Worley, Tetrahedron **26**, 4109 (1970); S. F. Nelsen and J. M. Buschek, J. Am. Chem. Soc. **96**, 2392 (1974).

[31] D. C. Frost, S. T. Lee, C. A. McDowell, N. P. C. Westwood, J. Chem. Phys. **64**, 4719 (1976).

[32] C. LaLau, in *Advances in Analytical Chemistry and Instrumentation*, Vol 8, edited by A. L. Burlingame (Wiley, Newark, 1970) p. 93; C. N. Burrous, A. J. Lieber, and V. T. Zaviantseff, Rev. Sci. Instrum. **38**, 1477 (1967).

[33] T. D. Märk, Z. Naturforsch. Teil A **32**, 1559 (1977).

[34] J. B. Anderson, R. P. Andres, and J. B. Fenn, Adv. Chem. Phys. **10**, 275 (1966); A. Kantrowitz and J. Grey, Rev. Sci. Instrum. **22**, 328 (1951).

[35] D. K. Sen Sharma and J. L. Franklin, Int. J. Mass Spectrom. Ion Phys. **13**, 139 (1974).

[36] J. H. Beynon and J. R. Gilbert, in *Gas Phase Ion Chemistry*, Vol. 2, edited by M. T. Bowers (Academic, New York, 1979), p. 153.

[37] D. M. Mintz and T. Baer, J. Chem. Phys. **65**, 2407 (1976); S. M. Penn, C. C. Hayden, K. J. Carlson Muyskens, and F. F. Crim, *ibid.* **89**, 2909 (1988).

[38] J. L. Franklin, P. M. Hierl, and D. A. Whan, J. Chem. Phys. **47**, 3148 (1967).

[39] W. J. Moore, *Physical Chemistry*, 4th ed. (Prentice-Hall, Englewood Cliffs, 1972), p. 130 ff.

[40] W. H. Press, B. P. Flannery, S. A. Teukolsky, and W. T. Vetterling, *Numerical Recipes* (Cambridge University, New York, 1986), p. 381 ff.

[41] J. Berkowitz, *Photoabsorption, Photoionization, and Photoelectron Spectroscopy* (Academic, New York, 1979), p. 265–71.

[42] M. S. Banna, H. Kossman, and V. Schmidt, Chem. Phys. **114**, 157 (1987).

[43] G. Bieri, L. Åsbrink, and W. von Niessen, J. Electron Spectrosc. **27**, 129 (1982).

[44] A. W. Potts and W. C. Price, Proc. R. Soc. London, Ser. A **326**, 181 (1972).

[45] J. W. Rabalais, *Principles of Ultraviolet Photoelectron Spectroscopy* (Wiley, New York, 1977), p. 89.

[46] C. Krier, M. Th. Praet, and J. C. Lorquet, J. Chem. Phys. **82**, 4073 (1985); A. R. Rossi and P. Avouris, *ibid.* **79**, 3413 (1983); H. Köppel, L. S. Cederbaum, W. Domcke, and W. von Niessen, Mol. Phys. **35**, 1283 (1978).

[47] B. L. Carnahan, W. W. Kao, and E. C. Zipf, J. Chem. Phys. **74**, 5149 (1981).

[48] J. Kurawaki and T. Ogawa, Chem. Phys. **86**, 295 (1984).

[49] Fragment ion KE ϵ_i is related to center-of-mass (c.m.) KE $\epsilon_{i,\mathrm{c.m.}}$ by the relation $\epsilon_i = \epsilon_{i,\mathrm{c.m.}}[m_n/(m_i+m_n)]$, where m_i and m_n are the ion and neutral fragment masses, respectively.

[50] N. Ohashi, W. J. Lafferty, and W. B. Olson, J. Mol. Spectrosc. **117**, 119 (1986); N. Ohashi and J. T. Hougen, *ibid.* **112**, 384 (1985); N. Tanaka, Y. Hamada, Y. Sugawara, M. Tsuboi, S. Kato, and K. Morokuma, *ibid.* **99**, 245 (1983).

[51] A. H. Cowley, D. J. Mitchell, M.-H. Whangbo, and S. Wolfe, J. Am. Chem. Soc. **101**, 5224 (1979); L. Radom, W. J. Hehre, and J. A. Pople, *ibid.* **94**, 2371 (1972); L. Pedersen and K. Morokuma, J. Chem. Phys. **46**, 3941 (1967); E. C. Wagner, Theor. Chim. Acta **23**, 115 (1971).

[52] J. O. Jarvie and A. Rauk, Can. J. Chem. **52**, 2785 (1974); J. O. Jarvie, A. Rauk, and C. Edmiston, *ibid.* **52**, 2778 (1974).

[53] S. F. Nelsen, S. C. Blackstock, N. P. Yumibe, T. B. Frigo, J. E. Carpenter, and Frank Weinhold, J. Am. Chem. Soc. **107**, 143 (1985); S. F. Nelsen, Acc. Chem. Res. **14**, 131 (1981); S. F. Nelsen, G. R. Weisman, P. J. Hintz, D. Olp, and M. R. Fahey, J. Am. Chem. Soc. **96**, 2196 (1974).

[54] E. Hayon and M. Simic, J. Am. Chem. Soc. **94**, 42 (1972).

[55] W. H. Fink, D. C. Pan, and L. C. Allen, J. Chem. Phys. **47**, 895 (1967).

[56] S. F. Nelsen, M. R. Willi, and T. B. Frigo, J. Am. Chem. Soc. **106**, 7384 (1984); S. F. Nelsen, D. T. Rumack, and M. Meot-Ner (Mautner), J. Am. Chem. Soc. **110**, 7945 (1988); M. Meot-Ner (Mautner).

[57] J. A. Pople and L. A. Curtiss, J. Chem. Phys. **95**, 4385 (1991).

[58] S. G. Lias, J. E. Bartmess, J. F. Liebman, J. L. Holmes, R. D. Levin, and W. G. Mallard, J. Phys. Chem. Ref. Data **17**, 1 (1988).

[59] B. B. Brady and J. A. Syage (to be published).

[60] S. G. Lias, J. F. Liebman, and R. D. Levin, J. Phys. Chem. Ref. Data **13**, 695 (1984).

[61] D. F. McMillen and D. M. Golden, Ann. Rev. Phys. Chem. **33**, 493 (1982), and references therein.

[62] Ref. 45, p. 99 ff.

[63] R. B. Woodward and R. Hoffmann, *The Conservation of Orbital Symmetry* (Academic, New York, 1970).

[64] T. L. Gilchrist and R. C. Storr, *Organic Reactions and Orbital Symmetry* (Cambridge University, Cambridge, 1970); T. H. Lowry and K. S. Richardson, *Mechanism and Theory of Organic Chemistry* (Harper and Row, New York, 1976).

[65] T. Drewello, C. B. Lebrilla, H. Schwarz, and D. Stahl, Int J. Mass Spectrom. Ion Proc. **77**, R3 (1987).

[66] R. J. Crawford and K. Takagi, J. Am. Chem. Soc. **94**, 7406 (1972); S. Seltzer and F. T. Dunne, *ibid.* **87**, 2628 (1965).